NAVAL POSTGRADUATE SCHOOL

MONTEREY, CALIFORNIA

THESIS

PHYSICAL PROCESSES IN COASTAL STRATOCUMULUS CLOUDS FROM AIRCRAFT MEASUREMENTS DURING UPPEF 2012

by

Pamela A. Tellado

September 2013

Thesis Advisor: Qing Wang
Second Reader: Wendell Nuss

Approved for public release; distribution is unlimited

THIS PAGE INTENTIONALLY LEFT BLANK

REPORT DOCUMENTATION PAGE			Form Approved OMB No. 0704–0188
Public reporting burden for this collection of information is estimated to average 1 hour per response, including the time for reviewing instruction, searching existing data sources, gathering and maintaining the data needed, and completing and reviewing the collection of information. Send comments regarding this burden estimate or any other aspect of this collection of information, including suggestions for reducing this burden, to Washington headquarters Services, Directorate for Information Operations and Reports, 1215 Jefferson Davis Highway, Suite 1204, Arlington, VA 22202–4302, and to the Office of Management and Budget, Paperwork Reduction Project (0704–0188) Washington DC 20503.			
1. AGENCY USE ONLY *(Leave blank)*	**2. REPORT DATE** September 2013	**3. REPORT TYPE AND DATES COVERED** Master's Thesis	
4. TITLE AND SUBTITLE PHYSICAL PROCESSES IN COASTAL STRATOCUMULUS CLOUDS FROM AIRCRAFT MEASUREMENTS DURING UPPEF 2012		**5. FUNDING NUMBERS**	
6. AUTHOR(S) Pamela A. Tellado			
7. PERFORMING ORGANIZATION NAME(S) AND ADDRESS(ES) Naval Postgraduate School Monterey, CA 93943–5000		**8. PERFORMING ORGANIZATION REPORT NUMBER**	
9. SPONSORING /MONITORING AGENCY NAME(S) AND ADDRESS(ES) N/A		**10. SPONSORING/MONITORING AGENCY REPORT NUMBER**	
11. SUPPLEMENTARY NOTES The views expressed in this thesis are those of the author and do not reflect the official policy or position of the Department of Defense or the U.S.. Government. IRB Protocol number ____N/A____.			
12a. DISTRIBUTION / AVAILABILITY STATEMENT Approved for public release; distribution is unlimited		**12b. DISTRIBUTION CODE** A	

13. ABSTRACT (maximum 200 words)

The objective of this thesis was to perform the initial analysis of aircraft measurements from the field campaign of the Unified Physical Parameterization for Extended Forecast (UPPEF 2012). We examined the general characteristics of the observed stratocumulus-topped boundary layers and identified cases for future in-depth studies. We first determined the boundary layer heights from all sounding profiles. The results indicated the sharp westward increase of boundary layer height is limited to ~200 km offshore with an average slope of 2m per kilometer. Substantial west-east spatial variability of thermodynamic properties is also observed from vertical profiles. The sea surface temperature (SST) in the region varied significantly. Near surface measurements over the warm and cold SST regions for three cases were analyzed and compared. This research found that the small scale variability in the SST resulted in significant variation in the surface exchange of sensible and latent heat fluxes, and wind stress. Such variability makes it difficult to correctly parameterize surface fluxes. The presence of cool downdrafts in the upper cloud layer is evident in the joint probability density distribution and buoyancy flux profiles. The results from this research will guide future cloud parameterization scheme development in forecast models.

14. SUBJECT TERMS Stratocumulus Clouds, Marine Boundary Layer, UPPEF 2012, Aircraft measurements, SST front			**15. NUMBER OF PAGES** 95
			16. PRICE CODE
17. SECURITY CLASSIFICATION OF REPORT Unclassified	**18. SECURITY CLASSIFICATION OF THIS PAGE** Unclassified	**19. SECURITY CLASSIFICATION OF ABSTRACT** Unclassified	**20. LIMITATION OF ABSTRACT** UU

NSN 7540–01–280–5500

Standard Form 298 (Rev. 2–89)
Prescribed by ANSI Std. 239–18

THIS PAGE INTENTIONALLY LEFT BLANK

Approved for public release; distribution is unlimited

PHYSICAL PROCESSES IN COASTAL STRATOCUMULUS CLOUDS FROM AIRCRAFT MEASUREMENTS DURING UPPEF 2012

Pamela A. Tellado
Lieutenant Commander, United States Navy
B.S., U.S. Naval Academy, 2003

Submitted in partial fulfillment of the
requirements for the degree of

MASTER OF SCIENCE IN METEOROLOGY AND PHYSICAL OCEANOGRAPHY

from the

NAVAL POSTGRADUATE SCHOOL
September 2013

Author: Pamela A. Tellado

Approved by: Dr. Qing Wang
Thesis Advisor

Dr. Wendell Nuss
Second Reader

Dr. Wendell Nuss
Chair, Department of Meteorology

THIS PAGE INTENTIONALLY LEFT BLANK

ABSTRACT

The objective of this thesis was to perform the initial analysis of aircraft measurements from the field campaign of the Unified Physical Parameterization for Extended Forecast (UPPEF 2012). We examined the general characteristics of the observed stratocumulus-topped boundary layers and identified cases for future in-depth studies. We first determined the boundary layer heights from all sounding profiles. The results indicated the sharp westward increase of boundary layer height is limited to ~200 km offshore with an average slope of 2m per kilometer. Substantial west-east spatial variability of thermodynamic properties is also observed from vertical profiles. The sea surface temperature (SST) in the region varied significantly. Near surface measurements over the warm and cold SST regions for three cases were analyzed and compared. This research found that the small scale variability in the SST resulted in significant variation in the surface exchange of sensible and latent heat fluxes, and wind stress. Such variability makes it difficult to correctly parameterize surface fluxes. The presence of cool downdrafts in the upper cloud layer is evident in the joint probability density distribution and buoyancy flux profiles. The results from this research will guide future cloud parameterization scheme development in forecast models.

THIS PAGE INTENTIONALLY LEFT BLANK

TABLE OF CONTENTS

LIST OF FIGURES

THIS PAGE INTENTIONALLY LEFT BLANK

LIST OF TABLES

THIS PAGE INTENTIONALLY LEFT BLANK

LIST OF ACRONYMS AND ABBREVIATIONS

ASTEX	Atlantic Stratocumulus Transition Experiment
BL	Boundary Layer
BLH	Boundary Layer Height
CIRPAS	Center for Interdisciplinary Remote-Piloted Aircraft Studies
CTEI	Cloud-Top Entrainment Instability
CTV	Controlled Towed Vehicle
DRI	Departmental Research Initiative
DYCOMS-II	Second Dynamics and Chemistry of Marine Stratocumulus
EIL	Entrainment Interfacial Layer
EPAC	Eastern Pacific
FIRE	Fire International satellite cloud climatology project Regional Experiment
FSSP	Forward Scatter Spectrometer Probe
G1SST	Global 1km Sea Surface Temperature
GCM	General Circulation Model
GOES	Geostationary Operational Environmental Satellite
IR	Infrared
LIDAR	Light Detection and Ranging
LHF	Latent Heat Flux
LWC	Liquid Water Content
MABL	Marine Atmospheric Boundary Layer
MBL	Marine Boundary Layer
MODIS	Moderate Resolution Imaging Spectroradiometer
NCAR	National Center for Atmospheric Research
NCEP	National Centers for Environmental Prediction
NOAA	National Oceanographic & Atmospheric Administration
NRL	Naval Research Laboratory
NSF	National Science Foundation
NWP	Numerical Weather Prediction
NWS	National Weather Service
ONR	Office of Naval Research
PBL	Planetary Boundary Layer
PCASP	Passive Cavity Aerosol Spectrometer Probe
PDF	Probability Distribution Function
ROMS	Regional Ocean Modeling System
SHF	Sensible Heat Flux
SLP	Sea Level Pressure
SML	Surface-based Mixed Layer
SST	Sea Surface Temperature
STBL	Stratocumulus Topped Boundary Layers
TKE	Turbulent Kinetic Energy
UCI	University of California, Irvine
UPPEF	Unified Physical Parameters for Extended Forecasts

THIS PAGE INTENTIONALLY LEFT BLANK

ACKNOWLEDGMENTS

I would like to especially thank Dr. Qing Wang for her expertise, patience, and guidance throughout this entire thesis process. She was instrumental in my success in completing this research. I would also like to thank Mr. Dick Lind for teaching me all about rawinsondes and how to launch them, and also for providing the data afterwards. I also want to extend my gratitude to John Kalogiros, Mary Jordan and Mike Cook for their MATLAB skills—there were some difficult codes that I could not have completed without their help. Bob Creasey also made significant contributions to my thesis—thank you for helping me learn how to program Google Earth files, and gather CSFR and RUC model data for the UPPEF 2012 analysis. I also want to thank Kurt Neilson and Dr. Wendell Nuss for their weather forecasting and satellite imagery support during the study. Djamal Khelif (UC, Irvine), Haf Jonsson (CIRPAS), and Anthony Bucholtz (NRL) provided essential aircraft data and input with the aircraft instrumentation set up during my research.

Most importantly, I would like to thank my husband, Ulysses, for his unwavering love and support, and my daughters, Lily and Melanie, for giving me such joy these past few years while finishing my master's degree.

THIS PAGE INTENTIONALLY LEFT BLANK

I. INTRODUCTION

A. STRATOCUMULUS-TOPPED BOUNDARY LAYERS AND MILITARY OPERATIONS

Stratocumulus clouds, derived from two Latin words meaning "layer" and "heap," are essentially low, individual convective elements that are composed in a layered form under a shallow, sharp temperature inversion. Stratocumulus topped boundary layers (STBL) are common over the oceans that are west of continents on the eastern part of a subtropical high, and over the Arctic Ocean in the summer. Stratocumulus clouds cover approximately 20% of the Earth's surface and greatly affect energy and radiation balances between the ocean and atmosphere. They are strong reflectors of incoming solar radiation and weak emitters of outgoing longwave radiation, which have a large impact on the Earth's radiative balance. Recent observations show that low clouds reduce the global annual radiation balance by an average of 15 Wm^{-2} (Klein and Hartmann 1993). There are few areas where these clouds are not important climatologically (Wood 2012). The ability to understand the complete details on the stratocumulus cloud processes is very difficult. Much research has developed and refined the theories behind the STBL, including an original proposal by Lilly (1968) known as the mixed layer theory (Brost et al. 1982) and is used as basis for other scientists.

Stratocumulus clouds have been studied using aircraft for the past ninety years. The first aircraft flight that researched stratocumulus clouds took place on September 10, 1923 (Kloesel 1992). This flight was conducted by the Naval Air Fleet in San Diego, CA with the goal of quantifying and forecasting humidity and temperature aloft. The data from the flight became a starting point for the Navy to recognize that the low stratocumulus cloud deck which primarily existed during summer months had great strategic importance. They expended many man-hours to research these regions of stratocumulus clouds. The cloud studies generally took place off the west coast of continents with cold ocean currents, such as the Californian coast, where eighty percent of the world's stratocumulus clouds exist (Wood 2012). Relatively recent extensive studies on stratocumulus clouds are Fire International Satellite Cloud Climatology Project

(ISCCP) Regional Experiment, or just called FIRE, in June-July 1987, Atlantic Stratocumulus Transition Experiment (ASTEX) in June 1992 (Kloesel 1992), and Second Dynamics and Chemistry of Marine Stratocumulus field study (DYCOMS-II) in July 2001 (Stevens et al. 2003). The most recent experiment is Unified Physical Parameters for Extended Forecast (UPPEF) in August-September 2012, which this thesis discusses in detail. The past research has given a solid qualitative understanding on formation, maintenance, and dissipation of stratocumulus clouds. However, there are still many uncertainties and in order to accurately parameterize the cloud, additional quantitative measurements are needed to model the net effect of all the physical processes involved.

In recent years, various research groups developed PDF-related cloud parameterizations for models, mostly using larger eddy simulations. However, few of the parameterizations are evaluated against the limited aircraft observations. It is considered that the PDF approach may lead to a unified cloud parameterization that would apply to persistent boundary layer clouds. Also, ensemble forecasts have recently become state-of-the-art, but can only define model uncertainty to a certain extent. It is known that most general circulation models (GCM) do not consistently model the cloud top interface effectively in the marine stratocumulus regions (Stevens 2002). Many of the physical processes in stratocumulus clouds occur on time and spatial scales much smaller than the GCM time step and grid size. Typically, the highest resolution numerical weather prediction (NWP) models have horizontal grid-box scales of a few kilometers, and the spatial scale of cloud formation and dissipation is at least one order of magnitude smaller. This shows the need for cloud processes to be parameterized as part of subgrid-scale processes. Subgrid-scale processes are defined as all processes that cannot be resolved explicitly with present or future models (Kalnay 2003). These processes include turbulent mixing, condensation, evaporation, friction, and radiation, and occur on scales from a few meters to a few hundred meters, which are all smaller than the current model resolution. Ultimately, enhanced model physics and realistic lower boundary conditions, such as sea surface temperature, will improve stratocumulus cloud and other subgrid-scale parameterizations.

Naval forces operate in many regions, whether close to coast in littoral regions or over the open ocean, and it is imperative to understand the battlespace environment, especially the marine boundary layers. The warfighter depends on accurate models to achieve mission success. In order for the Navy to properly deliver a complete and representative forecast model to operational forces, the boundary layer environment must be fully known. Most naval operations are conducted in the boundary layer—a shallow but dynamically active layer of the atmosphere. The boundary layer is also the layer with persistent turbulence as it directly interacts with the Earth's surface and contributes to most daily weather phenomena, such as precipitation, fog, significant temperature changes and cloud cover. Many naval missions, such as flight operations, sensor deployments and detection of electro-magnetic signals, communication, and ship tracking, are impacted when operating under solid stratocumulus clouds. Remote sensing, which is heavily relied on for many tactical military operations, is directly influenced by the presence of cloud cover. If the boundary layer characteristics are known, relevant information can be exploited and effectively portrayed to ensure mission success.

B. THESIS OBJECTIVES

During September 2012, extensive aircraft measurements were made off the coast of Monterey, CA as part of UPPEF 2012, which the Office of Naval Research (ONR) sponsored as a Departmental Research Initiative (DRI). UPPEF 2012 field measurement utilized the Twin Otter research aircraft operated by the Naval Postgraduate School (NPS) Center for Interdisciplinary Remotely-Piloted Aircraft Studies (CIRPAS) for twelve research flights, ten of which were made in cloudy boundary layers with various cloud fractions. In addition to NPS, the Naval Research Laboratory (NRL) in Monterey, CA and University of California, Irvine (UCI) also participated in UPPEF 2012. The goal of the experiment was to study the cloud structure, turbulence, and other related physical processes in broken stratocumulus using aircraft-based instruments and platforms.

This thesis work analyzes the UPPEF 2012 dataset in order to seek answers to some of the scientific questions listed in the earlier section. The ultimate goal is to help improve cloud parameterizations in forecast models. This research provides the initial analyses of the aircraft measurements from UPPEF 2012. The first step is to examine all

measurements and identify specific cases for focused in-depth analyses. A variety of data analyses methods is used including statistical analyses and spectral analyses, along with different graphical presentations are used to depict the vertical and horizontal variability of the cloud-topped marine boundary layer.

This thesis is structured as following. It begins with an introduction on the atmospheric boundary layer and physical processes within stratocumulus clouds. An overview of UPPEF 2012 is presented next, followed by an analysis of the data collected and used for this thesis research. Then, two case studies are presented on boundary layer variability and three cases are discussed showing the sea surface temperature variability. Next, the turbulence characteristics are analyzed in cloud and at low levels. Finally, conclusions are made with recommendations for future studies.

II. BACKGROUND

A. THE ATMOSPHERIC BOUNDARY LAYER

The lowest portion of the atmosphere is considered the atmospheric boundary layer (ABL), also known as the planetary boundary layer (PBL) or simply the boundary layer (BL). The BL is "part of the troposphere that is directly influenced by the presence of the earth's surface, and responds to surface forcing with a timescale of about an hour or less" (Stull 1988). It is extremely important to the climate, weather and air quality. However, the structure of the BL is often very complex. The BL height characterizes the vertical extent of mixing in the boundary layer and the level where momentum, water, and trace substances are exchanged with the free troposphere. The bottom boundary of the atmosphere is the Earth's surface. Atop the BL is a capping inversion, a stable layer between the BL below and the free atmosphere above, which prevents turbulence mixing into the deeper troposphere. Exchanges of pollutants and moisture with the free troposphere are conducted through entrainment at the BL top (Hobbs and Wallace 2006). Over the ocean, the BL is often referred to as the marine boundary layer (MBL). MBL tends to be cloud-topped with stratocumulus, cumulus, and stratus clouds (Hennemuth and Lammert 2005).

The BL height is a key parameter used in many models. There are many methods used to determine the BL height. Rawinsondes are commonly used to determine the BL height, since routine soundings are done worldwide with high accuracy and relatively low cost. Rawinsondes observe only on a single line (Hennemuth and Lammert 2005) but offer vertical profiles of temperature and humidity through the inversion and up to tens of kilometers in regions mostly inaccessible to humans (Flores et al. 2013). The BL height estimation for UPPEF 2012 uses primarily rawinsondes and aircraft measurements. Aircraft provide concurrent measurements of many variables that can be used to estimate the height (Seibert 2000). They are also well-suited to measure mean and turbulence quantities along horizontal legs at various height levels (Brost et al. 1982). The BL height is constantly changing both spatially and temporally depending on the geographic location, topography, surface cover, time of day, season, and weather patterns. The BL

can vertically extend from tens of meters to a few kilometers in various regions of the world (Stull 1988). It can even collapse and turn "upside down" in extremely stable conditions (Sun et al. 2002, 2004). In case of the STBL, the BL height is consistent with the cloud top height below the strong capping inversion (Hennemuth and Lammert 2005).

B. CONCEPTUAL MODEL OF THE CALIFORNIA MARINE BOUNDARY LAYER

The MBL varies significantly in the coastal region due to the complex interaction among the coastal topography, air-sea temperature and surface roughness contrast, and synoptic conditions. California is topographically diverse with mountains and valleys. To the west of the Sierra Nevada mountain range and the Central Valley lie the Coastal Ranges along the northern and central CA coastline. These include the Diablo Range, just east of San Francisco and the Santa Cruz Mountains located to the south of San Francisco. These mountain ranges are home to the giant redwoods, the tallest trees on the planet. The coastal mountain ranges affect the local surface wind flow and the boundary layer characteristics off the CA coast.

Beardsley et al. (1987) proposed a conceptual model meant to describe the mean summertime state of the lower atmosphere over the Eastern Pacific (EPAC) during periods of persistent northwesterly winds, shown in Figure 1. The model assumes a straight coast, with an adjacent closed coastal mountain range, to account for the Coastal Range. The domain is divided into three regions parallel to the coast: a nearshore zone (0–20km), an intermediate zone (20–200km), and an offshore zone (200–1500km). In the offshore zone, the marine inversion tilts slowly down toward the coast. Furthest west, near 1500km offshore, the inversion is at its maximum at 1500m and decreases to 300m as the intermediate zone is approached. The eastward tilt reflects the effect of the subsidence from the summertime EPAC high and north to northwesterly surface winds with speeds between 5–7.5 ms^{-1}. Stratus-type clouds and fog only occur below the inversion. In the intermediate zone, the surface wind is typically faster, about 10 ms^{-1}, off the northern CA coast than anywhere else along the U. S. west coast. The maximum wind speed in this area is partly due to the EPAC high located directly to the west of northern CA. Other factors are towards the Gulf of Alaska, synoptic features traveling to the east

often interrupt the tendency for the surface isobars to parallel the coast, and towards the south, as the CA coast turns eastward, large-scale divergence increases within the marine layer. The effect contributes to the maximum alongshore flow along the northern CA coast. There is also a diurnal variation in the wind, by 1 ms^{-1}, with the strongest northerly winds in the morning. Higher wind speeds in the intermediate zone imply that the marine layer must tilt more steeply toward the east by geostrophy.

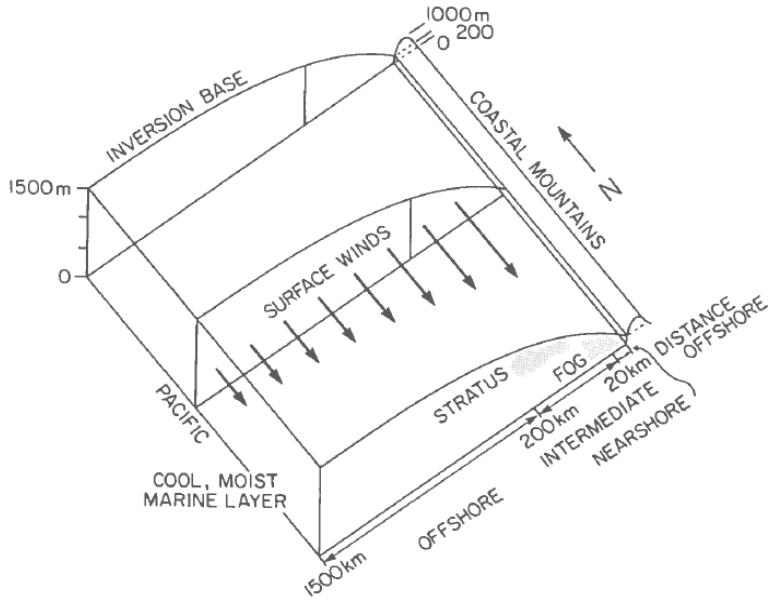

Figure 1. Conceptual model of summertime MBL over northeastern PAC during periods of persistent northerly winds (From Beardsley et al. 1987).

The nearshore zone is characterized by land-sea diurnal variability (Beardsley et al. 1987). A separate conceptual model is shown in Figure 2. The maximum variability occurs over the beach and decreases rapidly offshore. Over the narrow coastal plain, nighttime infrared (IR) cools and stabilizes the lower atmosphere, resulting in calm winds in the lower 50m over land. At night, the northwesterly winds weakly increase with height, from 50 m to the inversion, without any significant cross-coast flow. In the early morning, there is a sharp and level inversion and the maximum northwesterly wind is 20km offshore. After sunrise, the sun heats the surface and destabilizes the coastal air causing a weak density-driven cross-coast circulation to set in and the maximum alongshore wind to penetrate onshore. There is a weak return flow above the eroded

inversion and the subsidence branch of this circulation cause the inversion to decrease to a minimum height of 50–100 m over the beach (Beardsley et al. 1987). Inland, turbulent mixing and surface heating causes the inversion to lift slowly and diffuse. The maximum wind speed is located just below the base of the inversion offshore, while it is broadly located between the inversion base and the ground inland. As the sun goes down, the stability over land increases due to radiative cooling and the weak cross flow ceases.

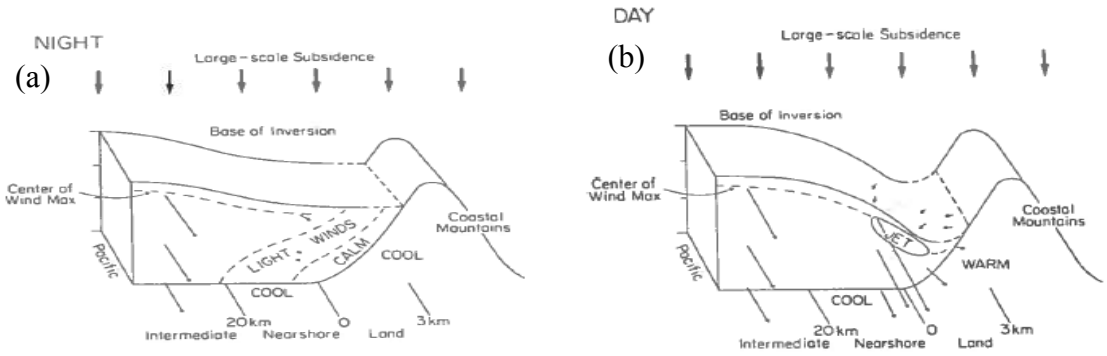

Figure 2. Conceptual model of variability of MBL height and low-level wind in the nearshore zone during (a) night and (b) day (From Beardsley et al. 1987).

C. SEPTEMBER CLIMATOLOGY OFF NORTHERN CALIFORNIA

1. Synoptic Pattern

The northeastern Pacific Ocean is dominated by a strong Eastern Pacific (EPAC) high during summer to early fall interacting with a heat low over the deserts of the southwestern United States causing a strong and persistent pressure gradient at the surface. The pressure gradient drives a steady northwesterly surface wind along the California coast. Figure 3a illustrates the climatological sea level pressure (SLP) and surface synoptic patterns: EPAC high, thermal low over the desert states, and the resulting surface pressure gradient. The surface wind for September is shown in Figure 3b, illustrating the strongest northwesterly wind at about 400 km offshore. These figures were generated using the National Weather Service (NWS) National Centers for Environmental Prediction and the National Science Foundation (NSF) National Center for Atmospheric Research (NCEP/NCAR) Reanalysis database located in the National

Oceanographic & Atmospheric Administration (NOAA) Physical Science Division and represents the average conditions for September with almost 30 year of data, from 1981–2010. Brost et al. (1982) notes this pressure gradient is probably the strongest and most persistent summertime pressure gradient observed in the entire North America.

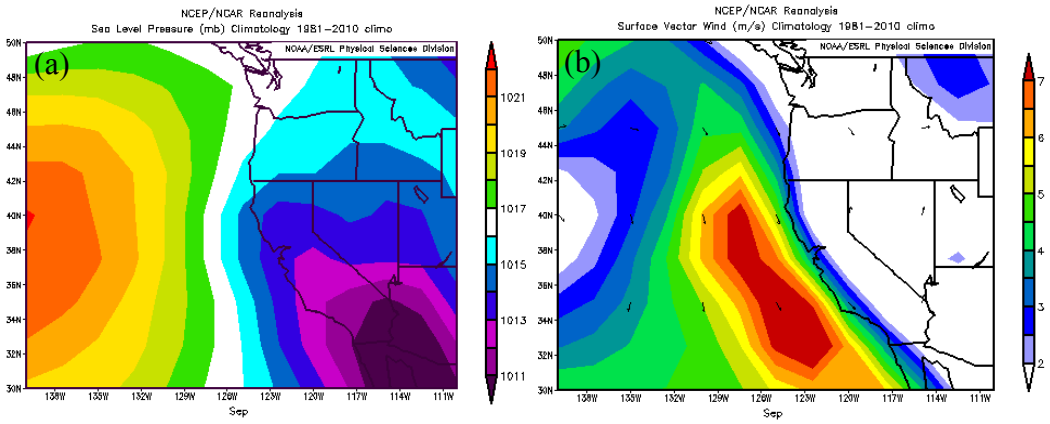

Figure 3. (a) Sea level pressure and (b) surface wind speed and wind vector climatology for September, generated from NCEP/NCAR reanalysis dataset.

The mean summer atmospheric regime is generally interrupted by five anomalous synoptic or mesoscale events (Beardsley et al. 1987). First, a strengthened gradient with enhanced northwesterly flow can occur for several days. This causes a stronger than normal, upwelling favorable wind event. Second, a weak, quick moving upper level trough passes and produces stronger than normal northwesterly, upwelling favorable winds, but limited to a day or so. Third, an internal Kelvin wave will produce a steady poleward progression of southerly winds, which is considered a wind relaxation or wind reversal event. The Kelvin wave causes the marine layer to rise along the coast and out to 50 km offshore. Satellite pictures show overcast stratus to mark the leading edge of the lifted marine layer with a clear area to the north. The clear area contains strong northerly winds and a lower marine layer. Kelvin waves typically travel 6 ms^{-1}. As the leading edge passes, the surface winds suddenly switch to southerly allowing overcast stratus to set in along the coast. A few days later, the Kelvin wave passes and winds suddenly reverse back to northerly. Fourth, another wind reversal event is caused by alongshelf southerly winds developing inshore along the northern CA coast. This event is contributed to

coastally trapped gravity currents that form at the southern CA coast and surge northward. This wind reversal is limited to a coastal zone of less than 100km wide. Along the coast, the inversion rises in spurts with the onset of the southerly winds and overcast stratus develops in the raised inversion. When the event ends, the inversion height decreases and the wind returns to normal. Finally, the smallest scale wind reversal occurs for a few hours in the morning and only in the very nearshore zone.

2. Sea Surface Temperature (SST) Characteristics

SST strongly affects the earth's climate and radiation budget, and influences cloud cover and turbulent heat fluxes. California is known to have relatively cold coastal waters. The combined Coriolis effect and the wind stress from the maximum northwesterly alongshore wind off central and northern CA pushes the upper layer of water offshore to the southwest. The upper layer of water is replaced by cold bottom water through upwelling, resulting in low sea surface temperatures immediately offshore. The marine atmospheric boundary layer (MABL) over the cool SST region is generally colder and prone to saturation, especially between Point Conception and Cape Blanco (Beardsley et al. 1987). The combination of increased subsidence from the strong EPAC high and a cool MABL creates a very strong inversion at the MABL top during the summertime, which in turn traps the cool, moist air close to the surface, causing much of the Californian coastline to be covered with thick stratus or fog for a majority of the day.

Climatologically, during September, SST is lowest just off the CA coast and increases to the southwest, as depicted in Figure 4, generated using NCEP/NCAR reanalysis database. The upwelled water near the coast is much colder (less than 15 °C) than the water offshore and sharp ocean fronts often occur as a boundary between the warm and cold water masses as seen from daily SST fields.

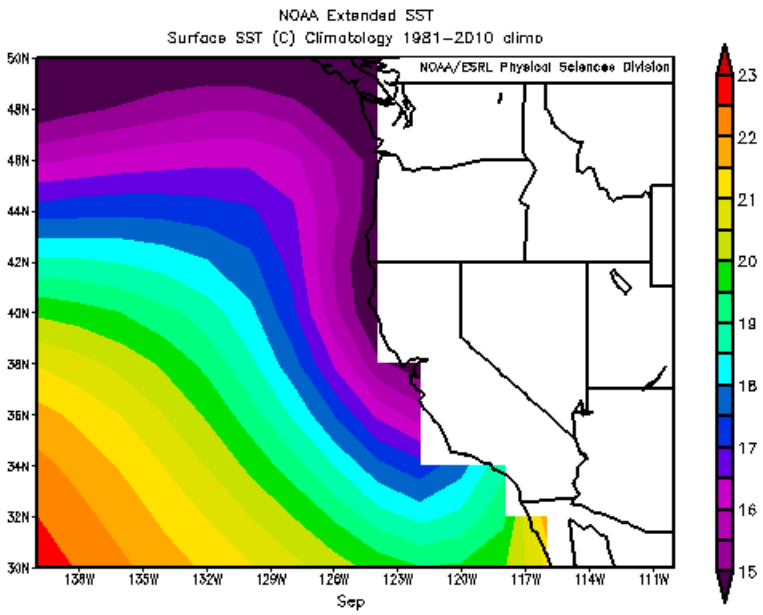

Figure 4. September SST climatology using NCEP/NCAR reanalysis database.

Filaments, also known as squirts, plumes, and tongues, can also occur and affect the BL. Upwelling filaments originate on the CA shelf and are narrow jets that advect cold coastal water several hundreds of kilometers offshore (Flament et al. 1985). There are three types of water across a filament: high-salinity warm water to the south, low-salinity warmer water to the north, and cold lower-salinity water in the filament's axis (Flament et al. 1985). The filament's boundaries are asymmetric. The southern boundary of cold water is constrained by a sharp front less than 1km wide and the northern boundary has a gradual transition from cold to warm water over 20km. Instabilities and strong turbulence can occur over the sharp front.

There are extensive sheets of stratocumulus in relatively shallow, well-mixed BL over cold SST. SST is one of the most important variables influencing cloud fraction in marine stratocumulus. It influences the stratocumulus clouds in two time scales (Hegg et al. 2004). On short time scales, higher SSTs are associated with higher heat and water vapor fluxes that moisten the MBL. They also produce warmer temperatures and greater water vapor mixing ratios at the cloud base, resulting in more liquid water content (LWC) and thicker, moister clouds. BL cloudiness is correlated with upstream SST on a timescale of approximately a day (Pincus et al. 1997). On longer time scales, higher SST

initiates the stratocumulus to cumulus transition and breaks up the cloud deck. Diurnal variations introduced by solar radiation can decouple the cloud layer from the surface during the day in these regions. The gradual increase of SST on a large scale, e.g., from the CA coast southwest toward Hawaii, deepens the boundary layer and eventually leads to permanent decoupling of the cloud layer from the surface-based mixed layer (SML) (e.g., Pincus et al. 1997, Bretherton et al. 1995). Moisture builds up in the SML which supports cumulus cloud growth from the top of the SML. Cumulus clouds either help maintain stratocumulus by supplying it with moisture from the SML or dissipate by enhancing the entrainment into the cloud layer (Wang and Lenschow 1995, Bretherton et al. 1995). A schematic diagram of the transition of stratocumulus to cumulus cloud is provided in Figure 5. UPPEF 2012 was primarily focused on the stratocumulus cloud in the shallow, well-mixed layer over cold SSTs off the CA coast.

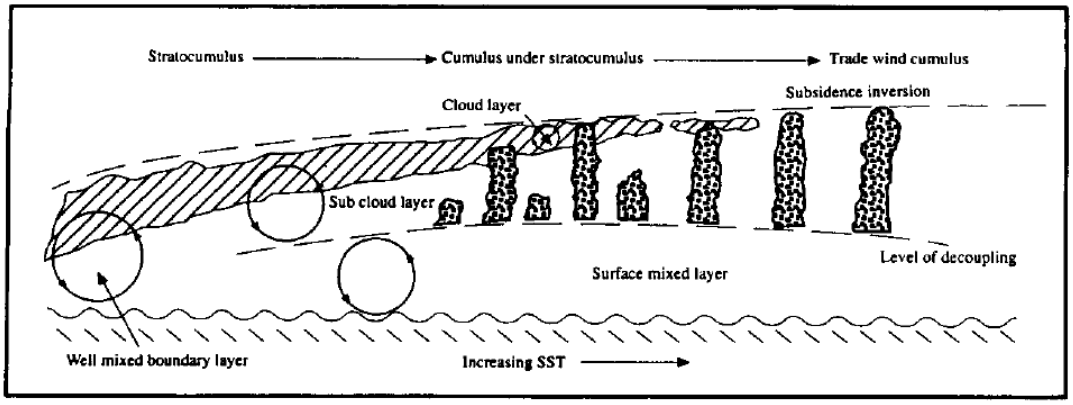

Figure 5. An illustration of the transition from stratocumulus to trade wind cumulus (From Bretherton et al. 1995).

3. Inversion Characteristics

There is a strong temperature inversion over most of the EPAC that clearly marks the boundary between subsiding dry, warm air above and cool, moist air in the turbulent, marine layer below. The inversion is in general thickest and has the greatest temperature difference between the top and base just off northern CA (Beardsley et al. 1987). Typically, the inversion is about 400 m over North and central CA coast, rising quickly to the west to a maximum of about 2000 m near Hawaii (Beardsley et al. 1987). According

to Brost et al. (1982), near the CA shore the BL is shallow, stably stratified, and foggy. Father out, it becomes deeper, near-neutral, and stratus or stratocumulus topped. Farther still, toward Hawaii (HI), the cloud layer breaks up into scattered cumulus (Figure 5). There is a north-south change in inversion height due largely to entrainment and mesoscale vertical motion. The east-west change in inversion slope is due to the average sea surface temperature increase to the west and weaker subsidence away from the center of the subtropical high. The inversion slope can cause large vertical wind shears (5–10 ms^{-1}) with winds being faster below the inversion than immediately above (Beardsley et al. 1987). The relatively low inversion in the stratocumulus-topped MABL forces the wind direction to be constant with height in the BL, with a jump in wind direction across the inversion (Brost et al. 1982). At the inversion, wind shear is large and produces turbulence and entrainment.

D. PHYSICAL PROCESSES IN THE STRATOCUMULUS-TOPPED BOUNDARY LAYER

1. General Characteristics

Low stratocumulus clouds are found primarily over the oceans and on the eastern side of the semi-permanent subtropical high pressure systems. Stratocumulus clouds form just below a strong temperature inversion below 1500 m in altitude (Wood 2012), which marks the marine boundary layer top over large areas of the oceans. They are also normally referred to as low-level clouds primarily driven by convective instability due to radiative cooling at the cloud top. The maximum cloud amount occurs during the summer months (June, July, and August) when the low-level thermal stability also peaks (Klein and Hartmann 1993). The clouds dissipate by processes, such as entrainment drying, decoupling, or drizzle or by transitioning to another cloud type (cumulus for example) (Wood 2012).

The vertical structure of the stratocumulus-topped boundary layer (STBL) is strongly tied to the associated stratocumulus clouds. Fractional cloud coverage is greatest when the STBL is moderately shallow (height is 500–1000m) and well mixed. Figure 6 shows typical vertical thermodynamic structures of water vapor (q) and liquid water

mixing ratios (q_l), equivalent potential temperature (θ_e) and temperature (T) for summertime shallow, well-mixed STBL corresponding to the photograph of solid stratocumulus clouds in Figure 7. The cloud top corresponds to the level that q_l decreases abruptly from its maximum with a strong T and θ_e inversion, and rapid decrease in q. The liquid water mixing ratio typically increases with height at a quasi-linear rate in stratocumulus layers, and is primarily affected by temperature and weakly dependent on pressure (Wood 2012). The boundary layer is below the shallow and sharp inversion normally less than 100m thick.

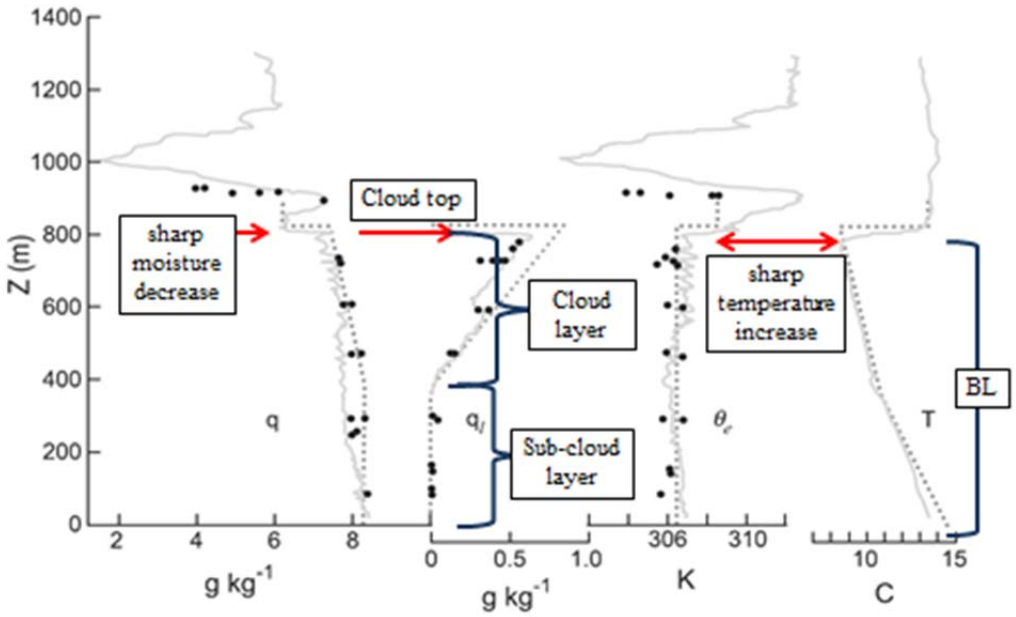

Figure 6. Typical thermodynamic vertical profiles of q, q_l, θ_e, and T for summertime shallow, well-mixed STBL. Dots depict horizontal leg means from constant level measurements. Significant layers and boundaries are labeled (After Nicholls 1984).

The STBL is capped by a shallow layer called the entrainment interfacial layer (EIL) which starts at the base of the inversion layer atop the cloud. This layer has strong gradients in temperature, humidity, and cloud liquid water. The universal defining feature of the EIL is the strong temperature increase (inversion) and moisture decrease with height (Figure 6). Virtual potential temperature (θ_v) and total water content (q_T) maybe strongly correlated in the EIL (Nicholls and Leighton 1986). In Nicholls and Leighton

(1986), the EIL is often subsaturated, there is a net negative buoyancy flux, and vertical velocity fluctuations are relatively small in this layer. However, the entrainment induced evaporative cooling may also result in strong cool downdrafts as illustrated in Wang and Albrecht (1994). The EIL is on the order of a few meters to tens of meters thick, but is highly variable within the same cloud. The difference between air properties at the top of the cloud layer and the EIL are usually so marked and the distance between the two layers is small, it is often represented by a discontinuity or jump. Nicholls and Leighton (1986) noticed that data from flight legs close to the cloud top had quite different characteristics than those found only a few tens of meters deeper in the cloud. Beneath the EIL, at a depth of about 50 m, negatively buoyant downdrafts are established, θ_v and q_T are often positively correlated, and vertical velocity variance increases. This suggests radiatively cooled downdrafts have combined some drier air from aloft during cloud top entrainment.

Figure 7. Photograph of a solid stratocumulus cloud top (From Wood 2012).

Low level marine stratocumulus clouds are important contributors to the earth's radiation budget. Stratocumulus clouds have a high albedo (strongly reflective) compared to the ocean. Areas with persistent stratocumulus, such as the California coast, absorb twenty percent less solar energy annually than other places at the same latitude (Hanson and Gruber 1982). Liquid water content (LWC) determines the cloud's optical properties

and is a critical link between cloud dynamics and radiative effects. As optical depth increases, more solar radiation is reflected to space, cooling the atmosphere and the surface. Pincus et al. (1997) showed that clouds with large optical thickness values in the morning time are unlikely to break up during the afternoon.

On any given day, there can be large and mesoscale variations in the stratocumulus cloud clearly visible in satellite imagery. One variation from solid cloud off the CA coast is a rift area. Rifts are areas with low reflectivity, distinctly cellular conditions seen from satellite, and advect with the BL winds (Sharon et al. 2006). Rift regions contain broken stratocumulus clouds surrounded by solid stratocumulus clouds. Another characteristic is that ship tracks have enhanced reflectivity in rift areas due to the increased aerosols from the ship exhaust and a decrease in drizzle. This enhanced reflectivity of ship tracks makes it easier to depict rifts in satellite images.

2. Key Physical Processes

The key physical processes that occur in the STBL are longwave cooling, solar heating, entrainment, turbulent mixing, latent heating, evaporative cooling, surface fluxes and wind shear, illustrated in Figure 8. Stratocumulus, a shallow convective cloud system, is maintained by the generation of buoyant instability by radiative cooling at the cloud top, which drives turbulent mixing to result in the observed temperature and humidity profiles, causes cloud top entrainment, and affects surface fluxes.

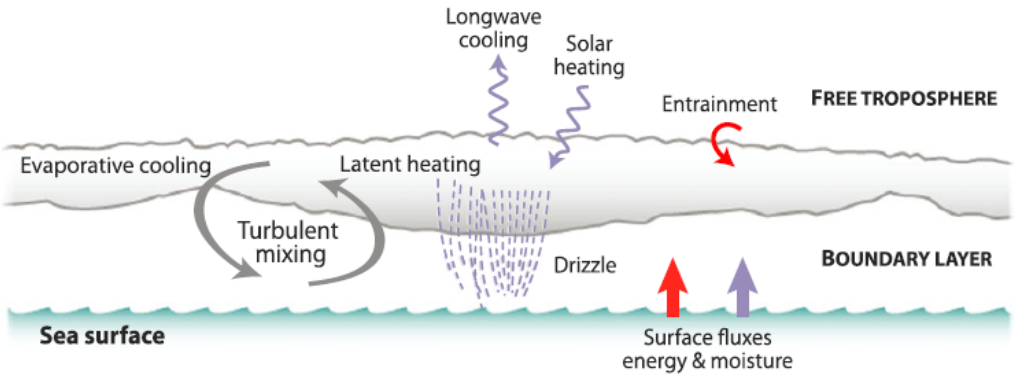

Figure 8. Schematic showing the key processes that occur in the STBL (From Wood 2012).

a. Longwave Cooling

Longwave cooling is the leading term in the STBL energy budget (Wood 2012), provides a major source of buoyancy that drives convective instability to generate and maintain turbulence in the cloud layer and below (Moeng 2000, Wood 2012). Most stratocumulus clouds contain a sufficiently abundant amount of liquid water so they are essentially opaque to longwave radiation. The longwave volume absorption coefficient increases quasi-linearly with q_l. Normally, the depth that the longwave radiation penetrates in stratocumulus cloud tops, with q_l>0.2 g kg^{-1}, is only a few meters to tens of meters. Stratocumulus clouds tend to occur under a dry free troposphere with downwelling longwave radiative fluxes just above the cloud top is less than the upwelling flux, by several tens to a little over 100 W m^{-2} (Wood 2012). No more than a few tens of meters down from the cloud top, the downwelling and upwelling fluxes are approximately equal. Thus, the upper few meters of the cloud experience strong longwave cooling. The average flux difference in this layer is 50–90 W m^{-2} (Nicholls and Leighton 1986, Wood 2012). Also, near the cloud base, net longwave flux convergence causes weak heating. Away from the cloud layer, the longwave flux divergence is small and does not significantly contribute to the net heating or cooling of the STBL. In addition, longwave cooling is considered a key dynamical element that drives overturning of convective circulations in the clouds.

b. Solar Heating

Solar heating, also called solar absorption, is another major component in the STBL energy budget (Wood 2012) and is the primary driver of the STBL diurnal cycle (Turton and Nicholls 1987, Wood 2012). The majority of solar absorption in cloud occurs in the near-infrared band of the electromagnetic spectrum. The fraction of the absorbed incoming solar radiation by stratocumulus can reach up to 15% (Wood 2012). The fractional absorption decreases with the solar zenith angle and increases with cloud optical depth (to a limit). Water droplet absorbs close to half of the solar radiation in the cloud layer. For all cloud optical depths and solar zenith angles, solar heating is largest at the cloud top due to strong scattering of solar radiation at the cloud top limits absorption

lower down. In most stratocumulus clouds that the liquid water content increases with height, solar heating decreases much slower down through the cloud layer than longwave cooling. Even in cases of strong solar insolation, the net effect of radiation acts to destabilize the cloud layer (Wood 2012) causing continued entrainment as the layer warms and decouples from the surface (Pincus et al. 1997).

c. Turbulent Mixing

Turbulent mixing homogenizes the boundary layer and tends to couple the layer to the surface which maintains the moisture supply to the cloud. The STBL's mean state is predominately shaped by turbulent fluxes of energy, water vapor, and liquid water. The turbulent kinetic energy (TKE) influences the entrainment rate of the free-tropospheric air into the STBL. Profiles of vertical turbulent fluxes are important to determine STBL properties. A classic depiction of the STBL is described by Lilly in 1968 as the mixed layer theory. Lilly's theory describes the vertical structure of fluxes necessary for maintaining a well-mixed layer. For a completely well-mixed layer, the vertical energy and moisture fluxes are linear functions of height. For non-precipitation mixed layers, the vertical turbulent flux of total water is also linear with height (Wood 2012). The primary generator of TKE in the STBL is the buoyancy flux, which is a maximum in the cloud layer. TKE is dissipative and not conserved. The boundary layer can be turbulent only if there are specific physical processes generating the turbulence. The TKE energy balance shows that buoyancy production is largest just below the cloud top and near the surface (Nicholls 1984). TKE is transported downward from the cloud top through turbulent mixing.

Buoyancy fluxes are caused by radiative cooling and enhanced by latent heating. In the STBL, latent heat release causes the buoyancy flux to increase just above the cloud base. The maximum buoyancy flux is located at the upper part of the cloud layer, implying that cloud top cooling is a dominant mechanism in buoyancy production. In lower levels of the BL, the buoyancy flux decreases and is small and can be slightly negative (Nicholls 1989). Radiative cooling at the cloud top results in negatively buoyant eddies and entrains drier air from above the boundary layer as they become downdrafts.

Negatively buoyant downdrafts are the primary convective elements in a cloud layer. Updrafts are warmer and have higher LWC than the downdrafts.

d. Entrainment

Entrainment can drastically change the thermodynamic structure of the STBL and lead to evaporation of the cloud (Moeng 2000). It is defined as the process that fluid is exchanged across a density interface bounding a region of turbulent flow (Nichols and Turton, 1986). The warm and dry air is entrained into the cloud layer, forming an entrainment parcel. The thermodynamics of the entrainment parcel is quite complicated and plays a key role in STBL evolution. Mixing with the dry inversion air results in subsaturation of the entrainment parcel and thus the evaporation of the cloud droplets. As a result, depletion of the cloud water was observed in the entrainment parcel (Wang and Albrecht 1994). When conditions are right, the entrainment parcels become negatively buoyant due to evaporative cooling, contributing to positive buoyancy flux in the entrainment parcel. This process is referred to as buoyancy reversal. Buoyancy reversal strengthens the entrainment by driving small scale turbulence near the cloud top, leading to positive feedback of entrainment, called cloud-top entrainment instability (CTEI). It was hypothesized that CTEI may cause rapid breakup of the cloud deck, but such rapid breakup has not been verified from observations. However, Moeng (2000) suggests that buoyancy reversal dominantly controls the cloud amount.

The entrainment rate is considered the most important parameter to determine the STBL's thermodynamic and cloud structure in climate models. Unfortunately, this variable is extremely difficult to quantify. The Dynamics and Chemistry of Marine Stratocumulus (DYCOMS-II) represents the most recent organized effort to quantify the entrainment rate. The reader is referred to Stevens et al. (2003) and the many DYCOMS-II related articles on the latest development regarding entrainment rate.

e. Wind and Surface Fluxes

Although stratocumulus clouds are often found over the cool upwelling coastal water, surface buoyancy flux maybe positive depending on the air-sea

temperature difference and thus contribute to turbulent mixing in the STBL (Wang 1993, de Roode and Duynkerke (1996). In general, the surface buoyancy flux is less than 10 Wm^{-2}, if not slightly negative. Over relatively warm ocean, the surface buoyancy flux is the source of turbulence in the decoupled STBL (de Roode and Duynkerke, 1996) .

The surface moisture flux is the main source of moisture into the BL. However, compared to the buoyancy reversal process, the net impact on cloud fraction and liquid water path from the surface is insignificant (Moeng 2000). The surface latent heat flux (LHF) is defined as the flux of heat from water evaporating at the Earth's surface and condensing as water vapor in the BL, with constant temperature. LHF is determined by the surface relative humidity, temperature, and wind speed (Wood 2012). In contrast to LHF, the surface sensible heat flux (SHF) is defined as the conductive heat flux from the Earth's surface to the atmosphere and is dependent on a change of temperature. Both LHF and SHF are a part of many key processes transporting energy from the Earth's surface to the atmosphere. All physical process in the STBL may affect the various surface fluxes and in turn affect the source of moisture in the BL.

Vertical shear of the mean wind in STBL are observed near the surface and often in the inversion atop the cloud layer. Brost et al. (1982) presented cases measured from the California coast where the driving force of turbulence are in boundary layer wind shear, not radiative cooling in the STBL. The shear in the inversion may modify entrainment mixing at the cloud top. Wang et al. (2008) and Moeng et al. (2005) both examined the shear effects across the STBL top using large eddy simulations (LES). They found that the local wind shear from individual eddies can also modify the entrainment process even in the case when the mean wind shear is negligibly small.

f. Precipitation

Frequently, stratocumulus clouds produce light precipitation in the form of drizzle (Nicholls and Leighton 1986; Wood 2012). Precipitation affects cloud fraction by removing water from the BL as drizzle at the surface and by moistening and cooling below the cloud as the falling drops evaporate (Pincus et al. 1997). Drizzle is found 20–40% of the time in persistent marine stratocumulus. VanZanten et al. (2004) suggests that

drizzle is more prevalent than previously thought and can even induce a transition in cloud structure. Higher precipitation rates are not due to a change in shape of the drizzle droplets, but are mainly caused by more frequent occurrence of larger drizzle drops. The rate of precipitation is higher at the cloud base than at the top, so it is often characterized by the cloud base drizzle rate. Drizzle stabilizes the STBL by warming the cloud layer. This also reduces turbulent mixing and increases stratification. Below the cloud base, drizzle quickly evaporates due to the small droplet size. The evaporation of drizzle in the sub-cloud layer is rather significant, even for shallow BL. Over both the land and the ocean, the maximum amount of drizzle occurs in the early morning when the cloud thickness is greatest (Wood 2012). Sharon et al. (2006) observed substantial differences in drizzle characteristics between the solid stratocumulus deck and rift areas. Drizzle is clearly more evident from observations in rifts than the surrounding solid cloud.

3. Diurnal Variability

Stratocumulus clouds exhibit a diurnal pattern, controlled by variation in solar insolation throughout the day. Maximum cloud coverage normally occurs at night (Skupniewicz et al. 1991). Betts (1990) examined the diurnal variation in the BL thermodynamic structure off the CA coast. In the morning after sunrise, the solar heating of the cloud layer results in decoupling and raises the cloud base. The cloud top does not rise significantly, the cloud is thinned and may result in fractional cloudiness (Pincus et al. 1997). Thus, the cloud is thinnest when the maximum amount of solar energy is absorbed. When the cloud is thinnest, it transmits the most solar radiation to the surface (Hanson and Gruber 1982).

THIS PAGE INTENTIONALLY LEFT BLANK

III. UPPEF 2012 MEASUREMENTS

A. UPPEF 2012 OVERVIEW

UPPEF 2012 deployed the CIRPAS Twin Otter in stratocumulus regimes off the CA coast in order to examine various aspects of BL cloud and turbulence parameterizations for applications in extended range forecast models. The statistical parameterization method using probability distribution functions (PDF) of dynamic and thermodynamic variables was targeted for cloudy boundary layers with various cloud fractions, focusing on broken stratocumulus cloud regimes. Twelve research flights by the CIRPAS Twin Otter, a total of fifty flight hours, were dedicated to make daytime comprehensive aircraft measurements of cloud and turbulence in, below, and above the stratocumulus cloud off the CA coast. The first ten flights were flown for the cloud mission and the last two flights for the LIDAR mission west of Monterey Bay in northern CA. The Controlled Towed Vehicle (CTV) was utilized for five of the twelve flights (Table 1), which provided a new measurement capability from past experiments. The CTV is designed to characterize surface fluxes as low as 10m above the surface while the Twin Otter made similar measurements at its flight level. However, the CTV data collected was not available for analysis for this thesis research.

The offshore region of northern and central CA coast is one of the most extensive STBL in the world, making it an excellent location to study stratocumulus clouds. Focusing on the multi-scale variability in the daytime stratocumulus cloud provided an opportunity to examine the relationship between multiple processes that need to be incorporated into the forecast models. Also, since the clouds tend to decouple from the surface layer during the afternoon, based on their diurnal variability, the optimal measurement time for studying cloud evolution is in the early afternoon along the CA coast. Also, the CIRPAS Twin Otter research aircraft is based at Marina, CA (just north of Monterey, CA) and has easy flight range of the stratocumulus clouds. A graphical representation of the flight tracks and location of the first ten flights for the cloud mission is shown in Figure 9. All twelve flights are summarized in Table 1, to include the flight number, date, time, duration, flight pattern, and any additional comments. A variety of

flight patterns, such as the L-pattern, U-pattern, S-pattern, box, and long linear transects, were used during UPPEF 2012 to sample the different boundary layer and cloud characteristics. Vertical stacks, spiral and slant path soundings, and zig zag horizontal/vertical transects were also utilized in flight to sample mesoscale and small scale variability within the boundary layer, mean radiation measurements above and in cloud, low level turbulence, and microphysics within the cloud layer.

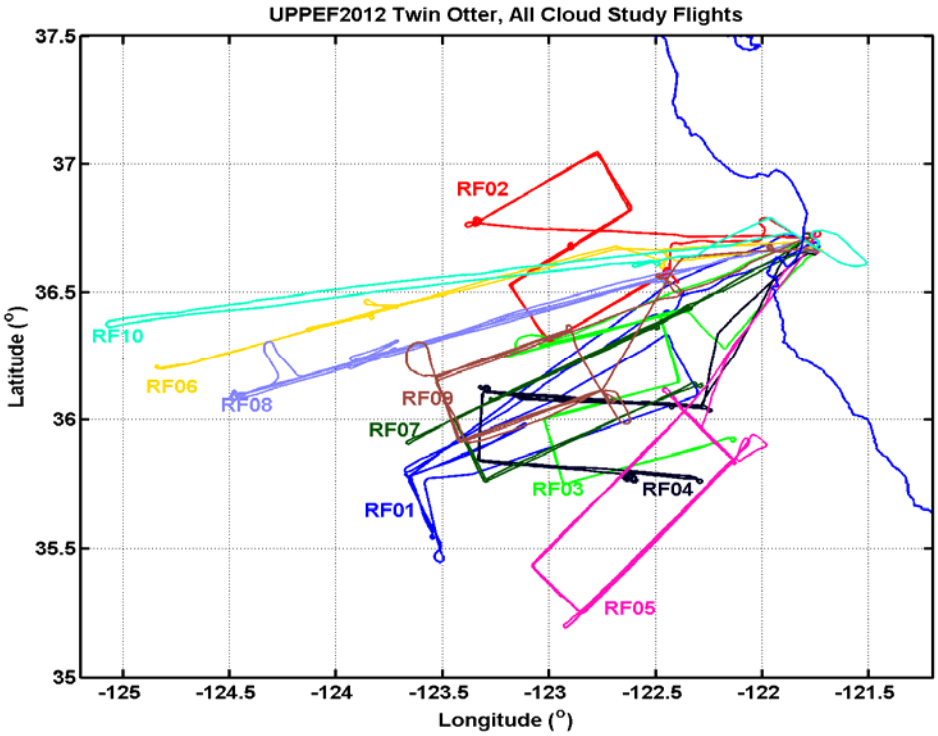

Figure 9. Flight tracks of the first ten UPPEF flights (RF01-RF10).

Each UPPEF flight was airborne for approximately 3.5 to 6 hours (see Table 1 for exact duration). Using the flight GPS measurements, individual legs are defined for full soundings, short soundings, and level legs. Full soundings are defined as legs from the surface or near surface to above the cloud top (and vice versa). Short soundings are defined as legs originating above the boundary layer top going into the boundary layer (vice versa) and level legs were the transits with the same altitude at constant heading (normally for five minutes or longer). Figure 11a shows the time series of aircraft altitude

(m) and heading (°) during RF01 overlaid each full sounding during flight. The full soundings are numbered consecutively, by order of time sequence. Their surface projections are shown in color lines overlaid on the entire flight track (Figure 11b). In the example shown in Figure 11 (RF01), five full soundings were completed. Figure 12 is the same as Figure 11, except it is for the level legs in RF01. Similar flight information was created and different types of legs were defined for all of the other eleven UPPEF 2012 flights.

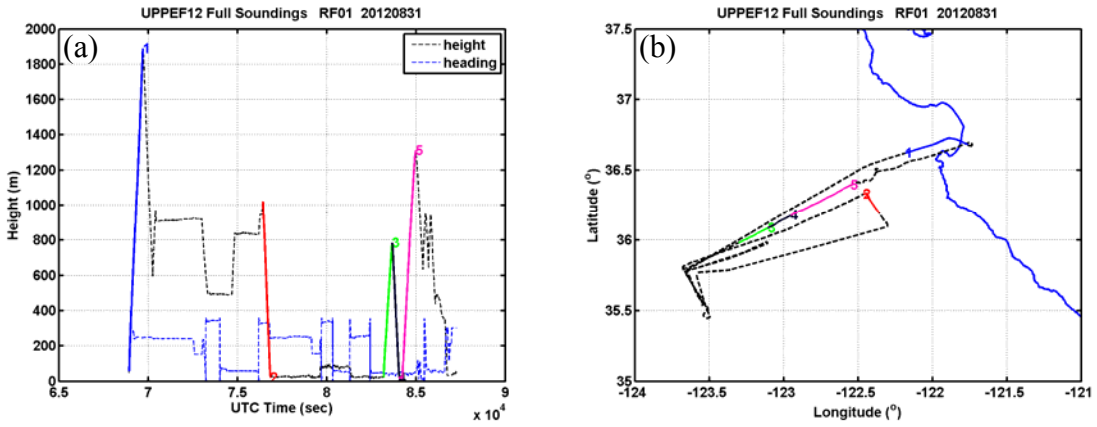

Figure 10. (a) Time series of height (m) and heading (°) showing full soundings overlaid on flight track; (b) Latitude/longitude plot showing full soundings overlaid on flight track for RF01.

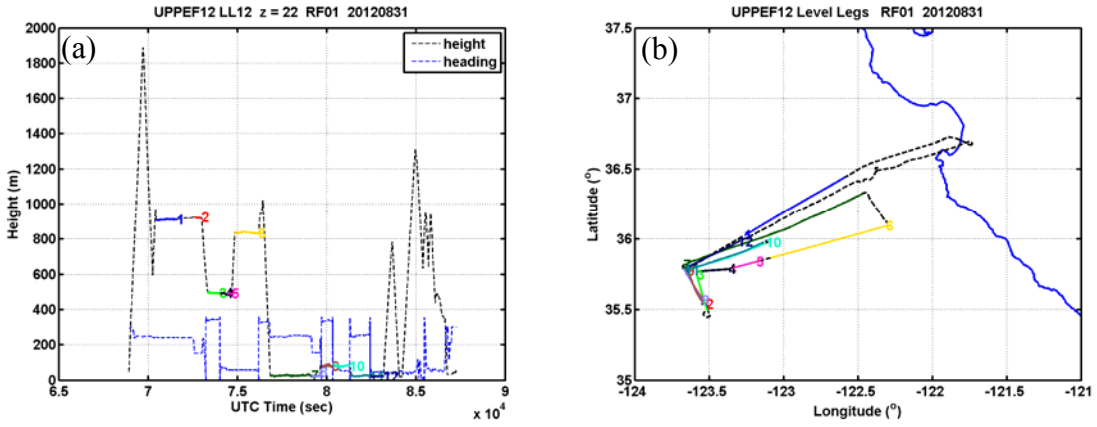

Figure 11. (a) Time series of height (m) and heading (°) showing level legs overlaid on flight track; (b) Latitude/longitude plot showing level legs overlaid on flight track for RF01.

Table 1. UPPEF 2012 Flight Summary

Flight #	Date	Takeoff-Landing Time (PDT)	Flight Duration	Major Flight Pattern	Comments
RF01	8/31/2012	1207-1705	5	L-pattern	Sampled at the clear/cloud boundary, ~ 20-30 kts wind. No CTV.
RF02	9/4/2012	1210-1720	5.2	S-pattern	Mesoscale variability in solid cloud cover at the beginning. Broken cloud layer. Multiple sounding were made. ~10 kts wind. No CTV.
RF03	9/6/2012	1228-1717	4.8	S-pattern	Thin solid/broken cloud cover. Weak and sometimes no wind, high SST. Twin Otter had a hard time staying in cloud because the cloud layer was very thin. No CTV.
RF04	9/7/2012	0941-1500	5.3	U-pattern	Gradual increase of cloud fraction from the coast to the west side of the U-pattern. U-pattern at 100 ft above surface for turbulence and cloud survey. Vertical stack in the cross-win direction at four levels below the cloud top. More clearing later in the flight. No CTV.
RF05	9/11/2012	0953-1310	5.3	U/box-pattern	Solid cloud with visible roll structure. Large clearing to the north. Some strong wind to the west in the alongwind leg. Variable surface waves and swell. No CTV.
RF06	9/13/2012	1137-1507	3.5	Long linear transect	1-hour long straight leg to the west to capture mesoscale features and broken clouds further offshore. First mission of UPPEF with CTV.
RF07	9/17/2012	1022-1537	5.3	U-pattern	Persistent solid cloud with clear mesoscale features. Cross-wind leg of U-pattern is 90k to capture mesoscale features. No CTV.
RF08	9/19/2012	1102-1617	5.3	Long linear transect	Long linear transect going through cloud (near coast) to clear transition. Roll structure. CTV used.
RF09	9/20/2012	0910-1430	5.3	U-pattern	Thin cloud, dissipated later on. Most of the measurements were made in clear with some thin puffy clouds. CTV used.
RF10	9/26/2012	1006-1342	3.6	Linear	UPPEF cloud mission with CTV and with TODWL installed. Maximum flight duration is 3.6 hr in this configuration. Solid to broken cloud transition from coast to further west.
RF11/RF12	9/30/2012	0920-1636	5.8	Varied	Two flights on this day after several days of waiting for clear condition. These flights are not part of UPPEF 2012 cloud missions, but are part of EDMF study. Both with CTV. Wind lidar data not available for most of second flight due to high cabin temperature.

Upper air soundings are important for future modeling efforts to characterize the temperature, humidity, pressure, and wind at above boundary layer levels. For this

purpose, two VIASALA rawinsondes were launched for all flights from CIRPAS at the Marina municipal airport, except for the first two flights where only one rawinsonde was available. Examples of temperature and dew point vertical profiles from a sounding are shown in Figure 13 for RF01, RF02, and RF03. Figure 14 displays the corresponding wind speed and wind direction profiles. The inversion base and any significant features are annotated in each plot. As seen in Figure 14a-d, the air is much drier above the BL than below as indicated by the increased separation between temperature and dew point. This is the effect of the ocean surface as a general source of water vapor and the capping inversion. The rawinsonde from RF03 shows the air column from 4000–5000m to be nearly saturated (Figure 13c, 13d). For RF01, the temperature inversion was at 768m over Marina (at the ascent) and 808m over Salinas Valley (at the descent) (Figure 13a). The wind was northwesterly at the surface and a westerly wind maximum (7 ms^{-1}) was at 200m ASL. The wind speed varied from 2–7 ms^{-1} for the entire rawinsonde launch and the wind direction shifted from westerly in the BL to southerly above (Figure 14a). The temperature inversion for RF02 was at 360m, half the altitude of the first flight (Figure 13b). The launches from RF03, suggest high temporal variability of the BLH. The height of the inversion for the first launch was at 429m (Figure 13c) while the height 4.5 hours later was suppressed to 250-284m (Figure 13d).

There were two types of launches for UPPEF 2012. The first was designed to go 'up and down' in order to get a good depiction of the boundary layer and the downward soundings provide the low-level measurements away from any ship effects. Examples of this type are the balloon launch for RF01 and the second launch during RF03, as indicated in Figure 14. The second type is a synoptic sounding, to go "up only," in order to get data from the entire troposphere. Examples are the balloon launches for RF02 and the first for RF03. In the wind profiles, the upper level jet is seen in the synoptic soundings (Figure 14b, 14c), which the "up and down" profiles for low levels did not capture (Figure 14a, 14d). The mid-level jet on the two days has similar magnitude, although the vertical variation leading to the jet core is rather different on these two days. Even though, the type of sounding is labeled "up only" data was still recorded as the rawinsonde descended in the atmosphere once the balloon was popped (no parachutes

were used for the descent). Similar plots were created for every rawinsonde launch during each flight.

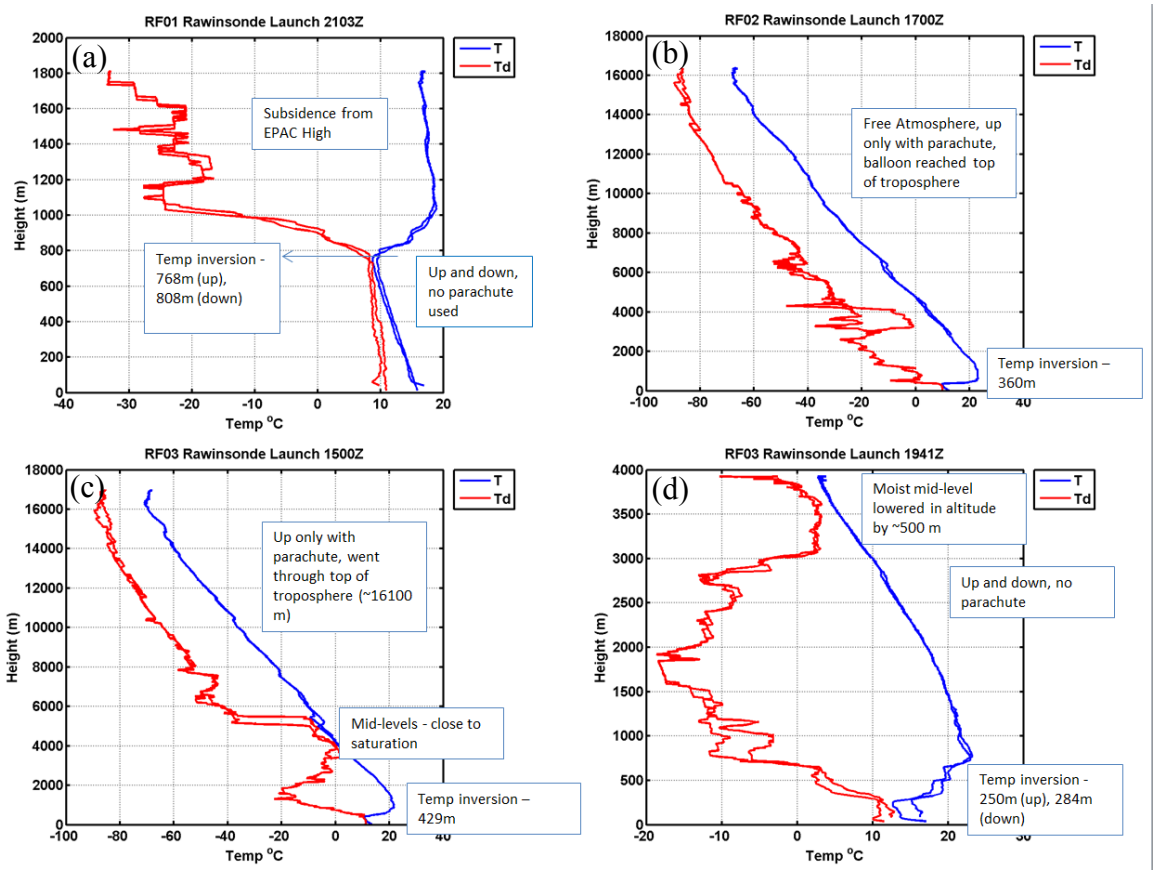

Figure 12. Annotated T and T_d profiles for (a) RF01, (b) RF02, (c) RF03, and (d) the second sounding of RF03 from rawinsonde launches.

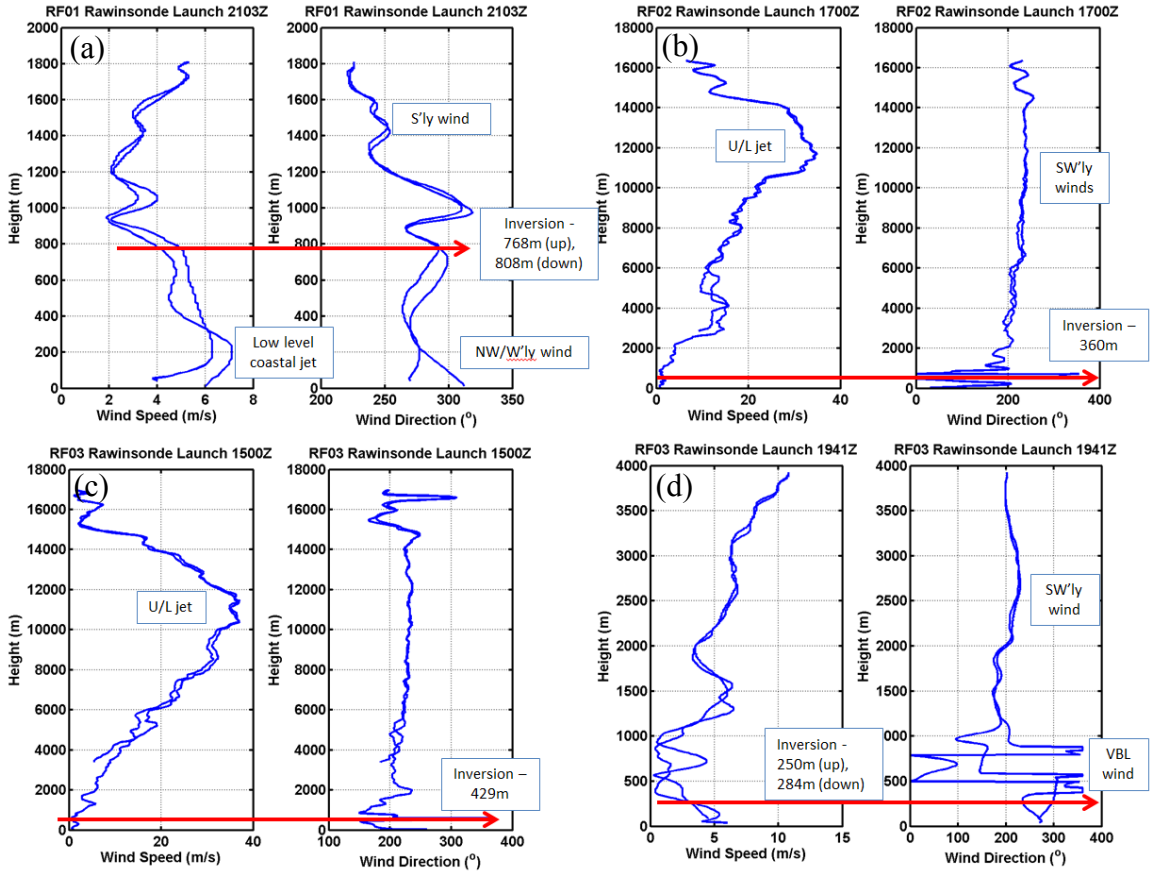

Figure 13. Annotated wind speed and direction vertical profiles for (a) RF01, (b) RF02, (c) RF03, and (d) the sounding of RF03 from rawinsonde launches.

B. CIRPAS TWIN OTTER INSTRUMENTATION AND MEASUREMENTS

The CIRPAS Twin Otter was outfitted with improved instrumentation for UPPEF 2012. There were four different GPS receivers, owned by CIRPAS and UCI, that provided flight path and navigation data. An improved 5-hole Radome gust probe measured wind and turbulence was installed. There were two fast-response Rosemont total temperature sensors from UCI and CIRPAS for redundancy and accuracy. Other sensors measured static and dynamic pressure, dew point, water vapor, absolute humidity, and carbon dioxide concentration. There were various upward and downward looking pyranometers measuring SST, up- and down-welling solar irradiance, up- and down-welling IR irradiance, and IR temperature. There were also sensors collecting aerosol and cloud properties, such as the Passive Cavity Aerosol Spectrometer Probe (PCASP) and the Forward Scatter Spectrometer Probe (FSSP). The measurement was

monitored in real-time at CIRPAS through satellite links. The meteorological data was processed and made available for the user from CIRPAS at 1 Hz and 10 Hz. Dr. Djamal Khelif, UC Irvine, also logged some of the fast sampling data separately and made them available for this research at 40 Hz. A photograph of the front of the Twin Otter is shown in Figure 15 annotated with the locations of the major instruments used during UPPEF 2012. The CIRPAS and UCI instruments used for UPPEF 2012, along with their description, measured variable(s), and data accuracy, are listed in Table 2. The onboard instrumentation is similar to previous Twin Otter research flights, as described by Khelif et al. (1999) and Khelif et al. (2005).

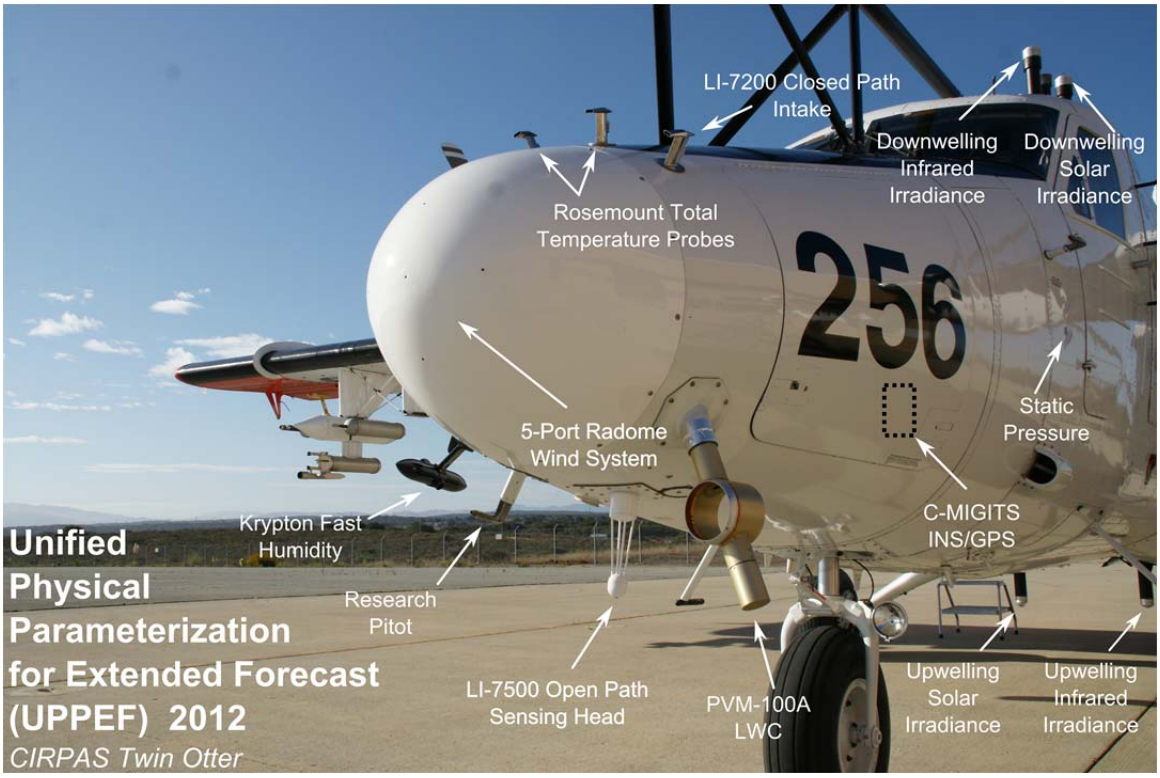

Figure 14. A photograph of CIRPAS Twin Otter showing placement of major instruments used during UPPEF 2012 (Courtesy of Djamal Khelif, University of California, Irvine)

Table 2. CIRPAS Twin Otter Instrument List used for UPPEF 2012 (input provided by Haflidi Jonsson, Djamal Khelif, and Anthony Bucholtz).

Instrument	Purpose	Description	Range
TANS Vector platform attitude (CIRPAS)	Flight Path/ Navigation	GPS, Pitch, Roll, Heading	
NovAtel GPS (CIRPAS)	Flight Path/ Navigation	GPS, Lat, Lon, Alt, ground speed and track	
C-MIGITS-III, GPS/INS (2 units, CIRPAS/UCI)	Flight Path/ Navigation	Lat, Lon, Alt, ground speed and track, pitch, roll, heading	
OXTS-RT3003 GPS/INS (UCI)	Flight Path/ Navigation	Lat, Lon, Alt, ground speed and track, pitch, roll, heading	had a OXTS base station to correct for post-flight differential GPS
Rosemount Total Temperature sensor (CIRPAS)	Meteorological parameters	Total Temperature	-50 to +50 °C
Rosemount Total Temperature sensor (UCI)	Meteorological parameters	Total Temperature	-60 to +40 °C
Edgetech Vigilant Dew Point Temperature sensor (CIRPAS)	Meteorological parameters	Chilled Mirror device	-50 to +50 °C
Setra 270 transducer- Static pressure sensor (CIRPAS)	Meteorological parameters	Static (barometric) pressure	600-1100 mb +/- .25 mb
Setra 270 transducer - total pressure sensor (CIRPAS)	Meteorological parameters	total (static + dynamic) pressure	600-1100 mb +/- .25 mb
Wind - Radome, flow angle probe (CIRPAS)	Meteorological parameters	Angle of attack and angle of sideslip differential pressures	-37.3-37.3 mb +/- .1 mb
Heiman, Heitronics KT 19.85 Pyrometer (CIRPAS)	Meteorological parameters	Sea surface temperature	-5 to 45 °C adjustable
Heitronics KT19.85 Upward-looking IR Temp (UCI)	Meteorological parameters	IR Temperature	-50 to +20 °C
Up-looking modified Kipp & Zonen CM-22 pyranometer (CIRPAS/NRL)	Meteorological parameters	Down-welling Solar Irradiance	0-1400 W m^{-2}
Down-looking modified Kipp & Zonen CM-22 pyranometer (CIRPAS/NRL)	Meteorological parameters	Up-welling Solar Irradiance	0-1400 W m^{-2}
Up-looking modified Kipp & Zonen CG-4 pyranometer (CIRPAS/NRL)	Meteorological parameters	Down-welling IR Irradiance	0-600 W m^{-2}
Down-looking modified Kipp & Zonen CG-4 pyranometer (CIRPAS/NRL)	Meteorological parameters	Up-welling IR Irradiance	0-600 W m^{-2}
Fast LI-COR 7500 H2O/CO2 Analyzer (UCI)	Meteorological parameters	Water vapor and CO2 densities	adjustable
Fast UCI- Modified KH2O (UCI)	Meteorological parameters	Absolute Humidity	adjustable
Passive Cavity Aerosol Spectrometer Probe (PCASP) - SPP200 (CIRPAS)	Aerosol properties	Particle Size Distribution	0.1 - 3.0 µm (100-3000 nm)
2 Condensation Particle Counters (TSI 3010) (CIRPAS)	Aerosol properties	Particle concentration	Dp > 0.01 µm (10 nm); Dp > 0.015 µm (15 nm)
Ultrafine Condensation Particle Counter (TSI 3025) (CIRPAS)	Aerosol properties	Particle concentration	Dp > 0.003 µm (3 nm)
Forward Scatter Spectrometer Probe (FSSP) - SPP100 (CIRPAS)	Cloud properties	Particle Size Distribution	2.0 - 30.0 µm
Cloud, Aerosol, and Precipitation Spectrometer (CAPS) (CIRPAS)	Cloud properties	Particle and Drop Size Distribution	0.5 – 50 µm (scatter) 25-1600 µm
PVM-100A probe (CIRPAS)	Cloud properties	Liquid Water Content of clouds	

C. SYNOPTIC CONDITIONS DURING UPPEF 2012

The synoptic conditions during the UPPEF 2012 measurement period are summarized in this section. On August 31, 2012, the synoptic pattern along the West Coast featured a quasi-stationary 500-mb trough axis situated along the coast in a north-south orientation, causing strong onshore flow. The EPAC High was located to the west of California and Oregon border, and moving slowly ENE. During the night before, as the atmosphere stabilized, extensive solid marine stratocumulus with small horizontal cell structures developed all along the coast from Cape Mendocino, south and coastward of 125W. West of 125W, there were very deep stratocumulus clouds with large cell structures with a narrow clear gap separating the two marine stratocumulus regimes. Along the coast, cell sizes were on the order of a few kilometers, while west of 125W the cell sizes were around 50km in diameter. During RF01, the wind was primarily northwesterly in the BL. The Ft. Ord profiler showed a deep marine layer, with the inversion near 762m (2500ft).

Over the next few days, the upper level trough shifted its orientation to northeast-southwest. The EPAC High built to 1032mb, moved north to the west of the Oregon and Washington border, and tightened the surface pressure gradient over northern CA coast. A thermal trough set up over Nevada and northern CA extending from a thermal low over New Mexico. Tropical Storm (TS) John was a weak system that formed off the southwestern coast of Mexico on September 2, 2012. TS John weakened over the cool waters west of the Baja Peninsula on 4 September to a Tropical Depression (TD) and advected midlevel moisture into the UPPEF region. For the second flight, on September 4, 2012, a weak mid- to upper level low remained west of the northern CA coast, with an upper level ridge over the Rockies. There was a stable marine layer with heights over most of the coast near 365m (1200ft) and cloud cover extended well west of Monterey Bay past 125W. The cloud bases were quite low at sunrise and rapidly rose during the morning hours. By noon, clearing was evident everywhere inland of the beach except for the first couple of miles inland around Monterey and Marina. The surface winds were northwesterly at 5-7ms^{-1} offshore of Monterey Bay, while above the BL the winds shifted to southwesterly.

On 5–6 September 2012, a cut off upper level low formed west of Monterey Bay and moved slowly northeast. This movement pushed the weakened EPAC high north into the Gulf of Alaska. For the third flight, on September 6, 2012, the stable marine layer along the central CA coast deepened with an inversion height approximately 430m. By midday, the cloud layer eroded out from the coastline to nearly 50nm offshore. The cloud bases were initially near 60m (200ft) and lifted as the clouds in the nearshore region burned off. The western edge of a midlevel tropical moisture plume was located just west of Monterey Bay (also seen in the rawinsonde plots in Figure 13). Between the coastline and 130W, a weak surface eddy or gyre developed, with northeasterly surface wind flow from the Washington and Oregon border down to Cape Mendocino. South of Cape Mendocino, off Monterey Bay, the wind was west-northwesterly in the BL and southerly above. There was a weak cyclonic structure in the stratocumulus field from 35N and north to the Oregon border.

On 7 September 2012, for the fourth flight, the surface pressure gradients along the coast relaxed to a weak onshore pressure gradient with little north-to-south gradient. Winds were northwesterly in the BL, while above there was a weak southerly flow lowering the inversion height to around 250m. In the morning, there was strong surface warming due to clear, sunny skies along the coast extending westward to the ragged edge of the solid stratocumulus field roughly along 125W. The cloud boundary remained quasi-stationary throughout the night and appeared to be retreating slowly in the early morning hours. By 8 September 2012, the EPAC high weakened to 1020mb and then reformed west of southern CA. The following day, an amplified upper level ridge set up over northern Montana with a deep trough west of California. The longwave pattern then moved east and both the ridge and trough decreased in amplitude. By the afternoon of 11 September, and on the fifth flight, the EPAC high built to 1031mb and moved north of CA toward the Gulf of Alaska. A thermal trough set up over northern CA which extended from the thermal low over Arizona (desert region). The large surface EPAC high pressure in the Gulf of Alaska brought strong northeasterly winds along the coast southward from the WA/OR border to just north of San Francisco Bay. A wind reversal event with weak cyclonic, coastally trapped southerly flow occurred right along the immediate coast of

Monterey County. Further offshore, the winds were northwesterly in the BL along RF05's flight track. The inversion rose from the previous flight to 400–500m along the coast.

The upper level ridge moved into the Gulf of Alaska by 12 September 0600 UTC and continued to move east. A thermal trough set up again over northern CA by 1800UTC. On September 13, 2012, the sixth flight, a strong 500-mb ridge has amplified along the West Coast. The wind reversal continued with the southerly surge of cool, dense marine air that propagated northward out of the Monterey area. The Monterey area was under an area of strong, warm subsidence which has kept the marine layer along the coast compressed to approximately 300–350m. The winds were southeasterly above the inversion and light west-northwesterly in the MBL. There was an extensive stratocumulus deck, evident in satellite imagery, continued to hug the coastline. The early morning cloud bases were very low with dense fog inland. By early afternoon, the fog lifted and burned back toward the beaches.

During the next few days, the elongated EPAC High (1028mb) moved south from the Gulf of Alaska toward the Washington and Oregon border. The upper level ridge moved eastward away from the CA coast. On September 15, a weak trough over the EPAC moved east toward the west coast. By September 16, a 300mb ridge was over San Francisco and Monterey Bay area. During the seventh, eighth, and ninth flights, 17–20 September 2012, a Rex block formed with an upper level low west of the OR/CA border and an upper level ridge to the north. The boundary layer initially deepened to about 600m and widespread solid and broken stratocumulus coverage. There was little change in cloud cover with a very strong inversion that kept the stratocumulus layer firmly capped for the seventh flight. There was strong southerly flow aloft and light surface westerly winds along the coast. During the eighth flight, the solid stratocumulus cloud became broken and burned off inland during the afternoon, with the temperature inversion diffusing and falling to 400m along the coast. The marine layer was not well defined for this flight. The upper level southerly winds weakened substantially from the past flight and surface winds shifted northwesterly. During the ninth flight, there were mostly clear skies across the region, with small areas of stratus over coastal waters, with

similar inversion heights of 350–400m. Winds were northwesterly in the BL and westerly above.

By September 23 at 0600 UTC, the upper level low in the EPAC pushed through the Rex block and became cut off, as it was under the amplified upper level ridge and then moved slowly southeast over the next few days until it merged with the longwave pattern. On the tenth flight, on 26 September 2012, a highly amplified ridge covered the eastern Pacific Ocean with a deep trough over eastern North America. The deepened marine layer (400–500m) and onshore flow allowed stratus to penetrate inland and along the coast for the duration of the flight. At 500-mb, the decaying Rex-block with a high centered west of Baja California coupled with a weak low centered west of WA/OR border displaced the EPAC high south of its normal position and induced a cyclonic circulation in the stratocumulus cloud field. For the last two flights, on 30 September 2012, another Rex blocking pattern affected the Monterey Bay region, which was under a strong 500mb ridge. This strong ridge compressed the inversion along with warmer air aloft into a surface based inversion, less than a hundred meters deep along the coast; and even washed out the marine layer in many places, allowing for clear skies in the area. Winds were westerly at the surface veering to easterly aloft (up to 12000m).

D. CLOUD STRUCTURE VARIABILITY

Throughout September 2012, the cloud pattern varied from clear, broken, and solid stratocumulus cloud depending on the boundary layer and synoptic patterns that occurred. The MODIS images are shown in Figure 15 and represent the cloud conditions at approximately 2145UTC for each flight, except for RF11. RF11's flight occurred earlier in the morning and the MODIS time did not cover that time, so the GOES-15 visible image was used instead. During RF01, there was extensive stratocumulus cloud in the morning in Monterey Bay and along the coast. Throughout the day, the cloud dissipated from the Bay and to the south. The second flight had mainly solid stratocumulus cloud, with some breaks in cloud during the end of the flight. The clouds were broken in the S-pattern for the third flight, and clear near the coast. The cloud pattern for the fourth flight had larger cellular clouds in the westernmost legs and

primarily clear skies near the coast. The fifth flight appeared to have rifts in the western part of the track with solid cloud towards the coast. A long linear transect was flown for the sixth flight capturing the solid cloud near the coast, broken cloud in the middle, with more solid cloud to the west. The seventh flight had primarily large cellular structures in the U-pattern track, clearing near the coast. There was a strip of stratocumulus cloud in the eight flights, with clear conditions over land and west of the track. The ninth flight had fairly clear conditions and solid stratocumulus during the entire tenth flight. The last two flights were mostly clear, with few thin scattered clouds in the region.

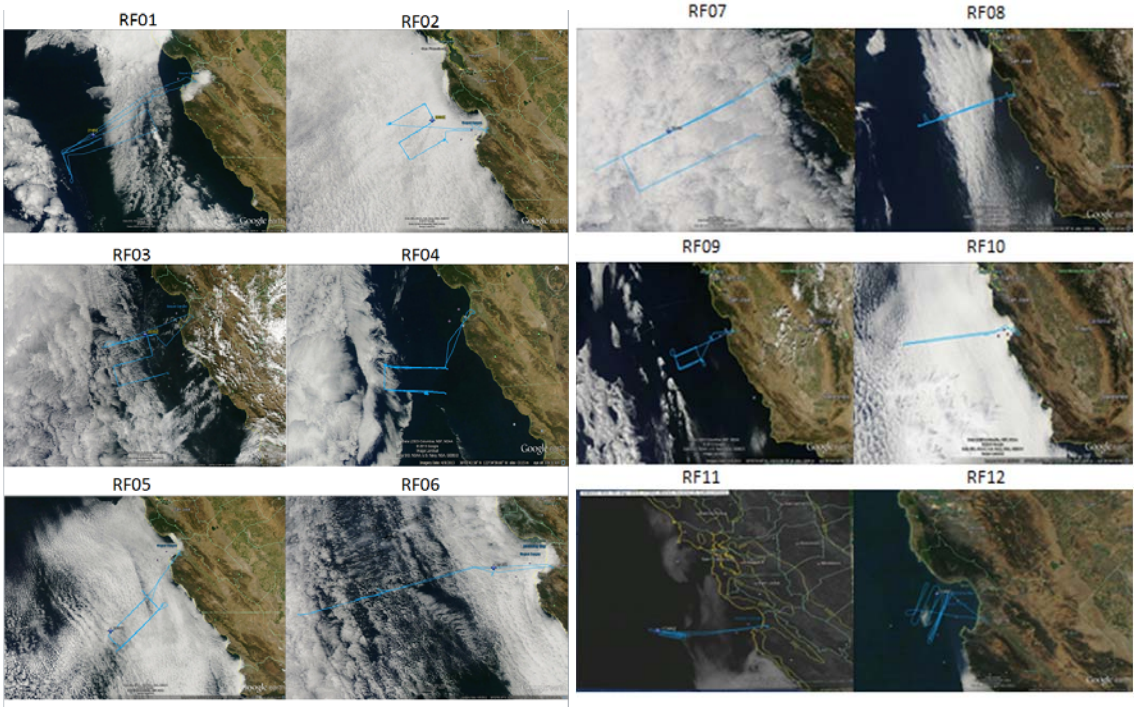

Figure 15. MODIS images capturing the cloud structure variability for the twelve flights (RF01-RF12) during UPPEF 2012. Blue lines indicate flight tracks.

E. MARINE BOUNDARY LAYER HEIGHT

According to Seidel et al. (2010), there are seven different methods to estimate PBL heights: the parcel method, level of potential temperature's maximum vertical gradient, the base of the elevated temperatures inversion, the top of the surface based inversion (SBI), the level of the minimum vertical gradient of specific humidity (q) or

relative humidity (RH) or refractivity (N). The parcel method evaluates the BL height by identifying the height at which θ_v is the same value aloft as at the surface (Seibert et al. 2000). It essentially determines the level where a hypothetical parcel of air will be in equilibrium with its surrounding environment. The base of an elevated temperature inversion serves as a cap to mixing below. The top of a SBI indicates a stable boundary layer and defines the top of the PBL. The other methods assume an unstable or neutral BL structure and are not used for stable conditions (Seidel et al. 2010). The method used while analyzing the UPPEF 2012 data research was a combination of all the methods, but primarily using the base of the temperature inversion, cloud top, minimum gradient in q, and turbulence measurements. The top of the SBI was used to determine the BL height for the last two flights. A combined BL height graphic of each UPPEF 2012 flight is displayed in Figure 16. Each flight is represented by a different symbol. The varying heights are represented by different colors, as shown in the graph's color bar. Each flight day exhibits a downward sloping of the BL height toward to the coast from the open ocean, as described in the conceptual model in Chapter II.

RF01 had the highest BL heights between 800–950m. RF02's BL heights decreased by about half and started near 350m at the coast increasing to 525m offshore. The BL heights in RF03 were 300m along the coast increasing to almost 700m offshore. The BL heights for RF04 and RF05 were around 700m offshore and at the coast approximately 400m. During RF06, the coastal BLH was at 300m, while at the furthest west leg was at a height of 720m. The BL heights during RF07 were considerably higher along the coast, at 600m, increasing to 800m offshore. There was about a 250m change during RF08 from 680m offshore near 124.5W to 430m along the coast. The BL heights near 123W rose considerably from RF08 from 600m to 800m. Along the coast BLH were similar near 400m. The tenth flight had a BL with gradual downward slope from 800-750m from 124-125W, then a much larger slope starting at 750m to 400m to the coast. The last two flights RF11 and RF12, had boundary layer heights considerably lower than all other flights, as there was a surface based inversion on this cloud free day, reducing the heights to below 200m.

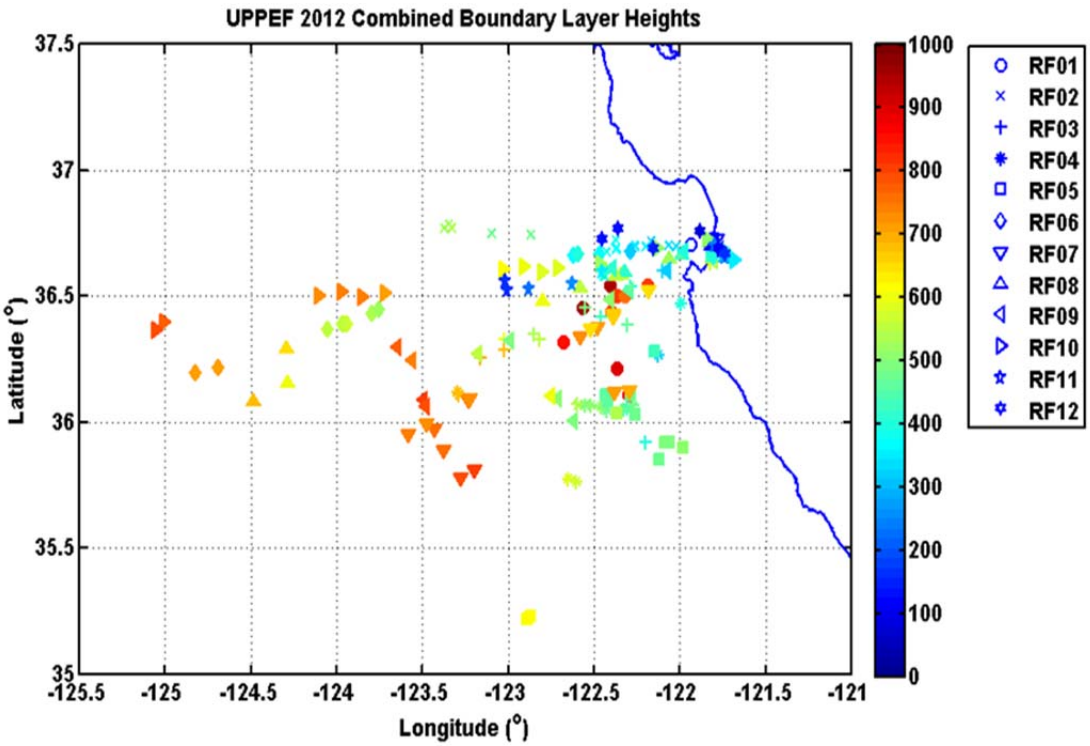

Figure 16. Combined BLH for UPPEF 2012 flights

IV. BOUNDARY LAYER AND CLOUD CHARACTERISTICS

A. BOUNDARY LAYER HEIGHT VARIABILITY

A common pattern in each flight was the downward slope of the boundary layer top towards the east (shoreward) as presented in Chapter II, Section B. The height of the boundary layer top changed as a result of synoptic and mesoscale pattern changes. Two of the ten flights, RF02 and RF10, were good examples of boundary layer variability in solid to broken cloud. This section will show satellite images from the Geostationary Operational Environmental Satellite (GOES) West, also called GOES-15, visible sensor and the Moderate Resolution Imaging Spectroradiometer (MODIS) sensor on the Terra polar orbiting, sun synchronous satellite, with resolutions of 1km and 250m, respectively. Boundary layer heights, vertical profiles, and cross sections of cloud liquid water (q_c), potential temperature (θ), specific humidity (q), wind speed, and wind direction from full soundings are also shown in this section.

1. RF02 (04 September 2012)

There was solid to broken stratocumulus cloud during the second flight, RF02, on 4 September 2012. Three consecutive GOES-15 visible satellite images off Monterey Bay (Figure 17), showing the spatial and temporal cloud variability for the duration of the flight. The cloud remained solid to broken with clearly identifiable mesoscale structure especially earlier in the flight. Total flight duration was 5.2 hours using mainly the S-pattern at two levels in cloud and two levels below. A zoomed in satellite image from the MODIS overlaid on Google Earth with the flight track and color coded full sounding legs are shown in Figure 18. All of the full sounding legs went through cloud top and provided valuable data in evaluating the boundary layer structure. Cloud liquid water (q_c), potential temperature (θ), specific humidity (q), wind speed, and wind direction, are plotted for each full sounding of RF02 in Figure 19. The profiles show the horizontal variability in the boundary layer. The cloud top is lowest near the coast and rises offshore and correlates well with the level of maximum θ increase, q decrease, and sometimes a change in wind speed or direction.

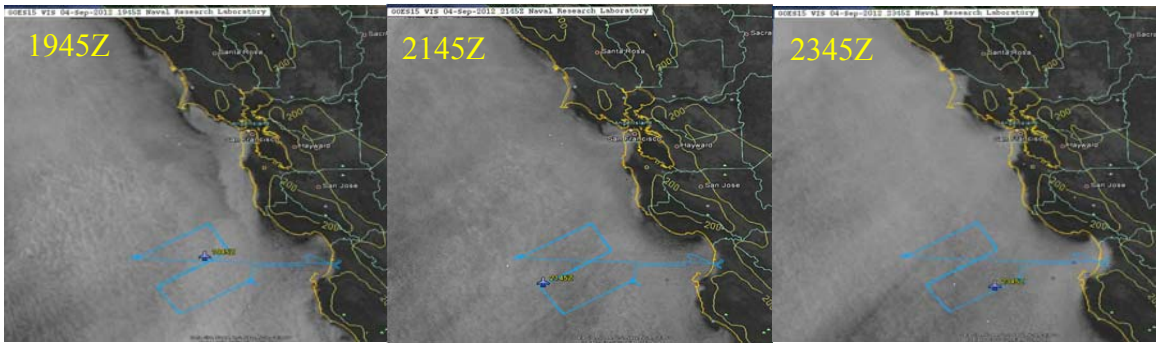

Figure 17. Three sequential GOES 15 satellite images on 4 September 2012 showing mostly solid cloud during RF02. Blue line is flight track, with plane icon indicating location of TO at time of satellite pass.

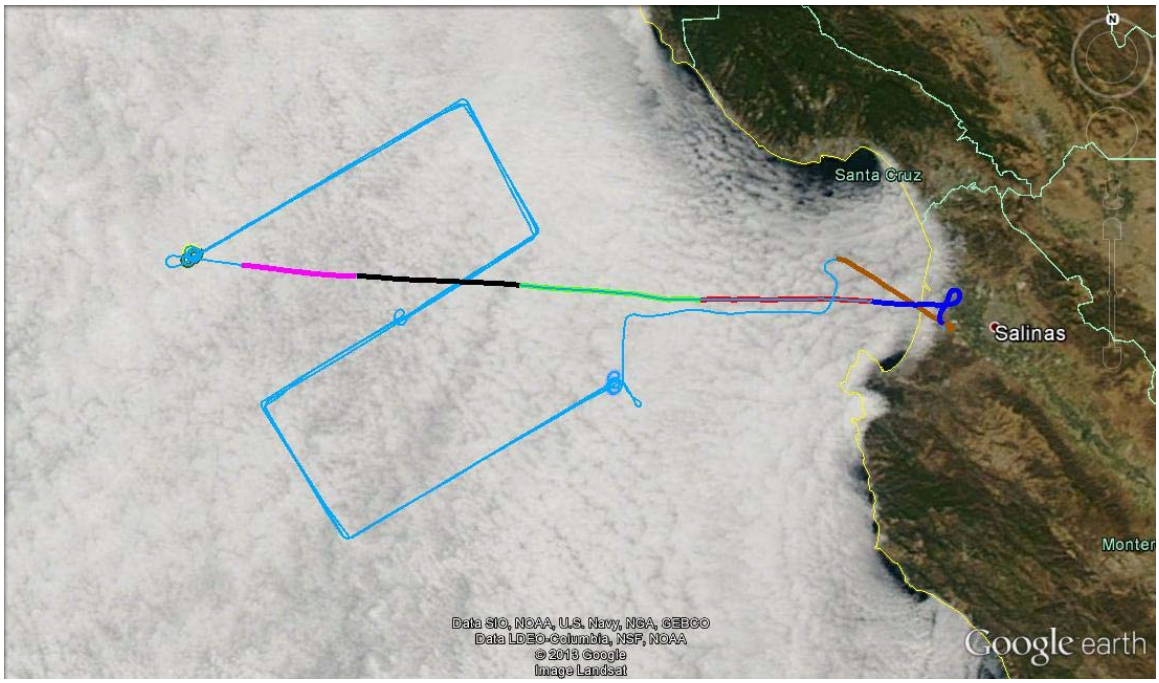

Figure 18. MODIS image on 4 September 2012 at 2045 UTC overlaid on Google Earth with RF02 flight track and the horizontal projection of all full soundings (FS1-FS9, colored via legend in Figure 19).

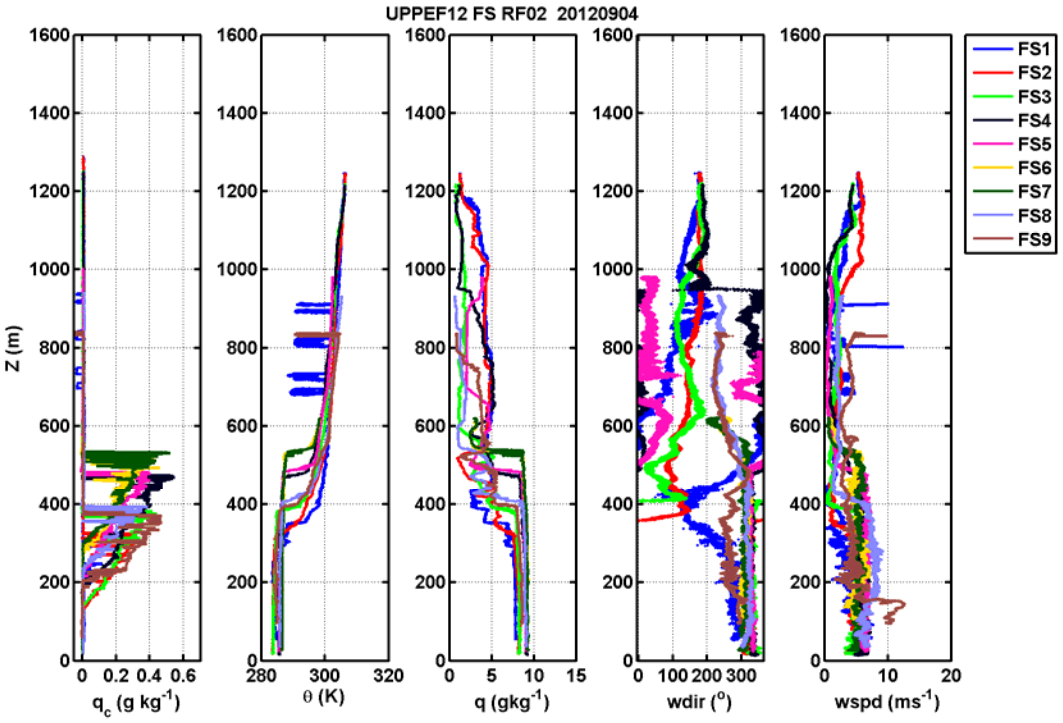

Figure 19. Vertical profiles for all full soundings in RF02, showing cloud and boundary layer variability in q_c, θ, q, wind speed, and wind direction. The spikes in FS1 and FS9 are due to interference with high frequency communications onboard the TO during takeoff and landing.

The boundary layer height was estimated from the vertical profiles as in Figure 19, and overlaid on the flight track in Figure 20. In the beginning of the flight, the boundary layer height was 269m from the take-off sounding. The height progressively increased offshore to 526m at the westernmost part of the track. As the TO headed back to shore near the end of the flight, the boundary layer decreased towards the East. The last full sounding from landing was at 375m, which is higher than the take off initial sounding, which is likely related to daytime heating of the surface over land.

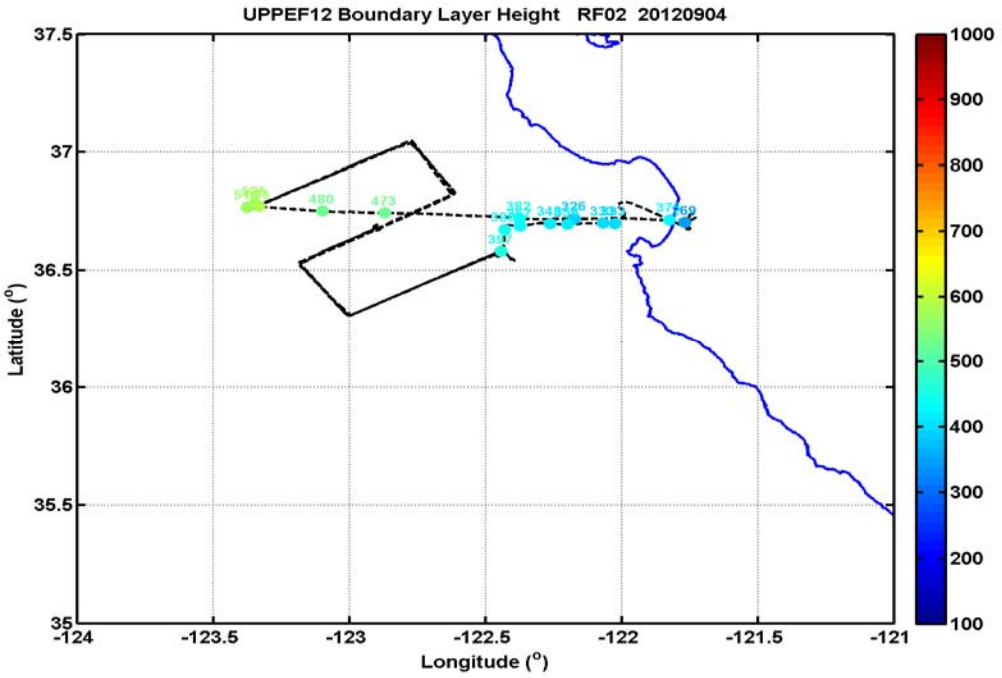

Figure 20. Boundary Layer heights for RF02. Dotted line represents flight track. Colored dots and numbers represent boundary layer height.

Liquid water content, specific humidity, temperature, and wind speed for FS1–FS5 and SS1 for RF02 are displayed using the contour plot function in MATLAB, in Figure 21. The red colors are the highest values and blue colors the lowest. The black solid line indicates the approximate slope for the BLH, estimated to be at 2 m per kilometer. The figure shows the upward tilt in the cloud top and base with cloud thickness slightly increasing offshore and thickest near 122.9W (FS4). The q_c increases from the base of the cloud with maximum values (>0.4 gkg^{-1}) near the cloud top. Specific humidity (Figure 21b) is high and fairly uniform with height in the boundary layer and through the cloud top, decreasing rapidly above the cloud top height. Higher moisture (7.2 gkg^{-1}) remained almost 200m above the boundary layer for FS5. There is also greater moisture in the boundary layer offshore (9 gkg^{-1}) than near the coast (7.1 gkg^{-1}) corresponding to higher SST away from the coast. At the top of the boundary layer, there is an inversion of almost 10K in approximately 50m depth. Potential temperature increases to approximately 305K above the boundary layer. The near-surface θ are about 2K colder near the coastal waters than offshore (Figures 20, 21c) and consistent with the

water temperature below. The first sounding was at takeoff from the Marina airport and experienced slightly higher θ (about 2K) then the upwelled coastal waters. The wind (Figure 21d) is strongest offshore (8 m s^{-1}) in the boundary layer, decreases to 2 m s^{-1} above the cloud layer. Each of the variables displayed typical stratocumulus profiles (e.g., Nicholls 1984).

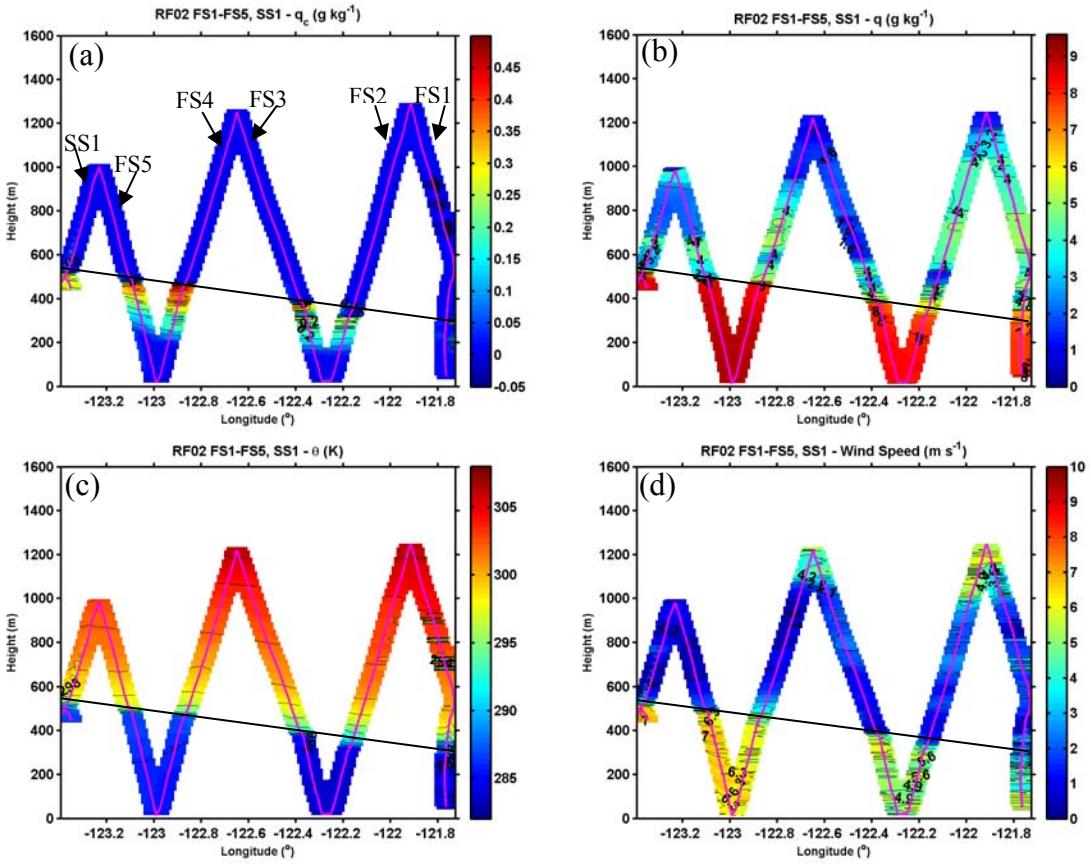

Figure 21. Contour plots for vertical profiles of (a) q_c, (b) q, (c) θ, and (d) wind speed for RF02 full soundings (FS1-FS5) and short soundings (SS1) combined. Flight track is represented by solid magenta line. Black line indicates slope of BL.

2. RF10 (26 September 2012)

The tenth flight, on 26 September 2012, was the last cloud study mission in typical summertime solid stratocumulus cloud. Figure 22 shows three consecutive GOES-15 visible satellite images of Monterey Bay. Solid cloud was throughout the

duration of RF10. Long linear transects were flown both in cloud and near the surface to get a full boundary layer picture. A MODIS image at 2145 UTC, with RF10 flight track overlaid and the Full soundings color coded, is presented in Figure 23. Roll structures in cloud aligned with the predominant northwesterly wind direction are apparent in all satellite images. West of the flight track the cloud is broken, while the cloud is solid for the entire flight track to the coast and clears over land.

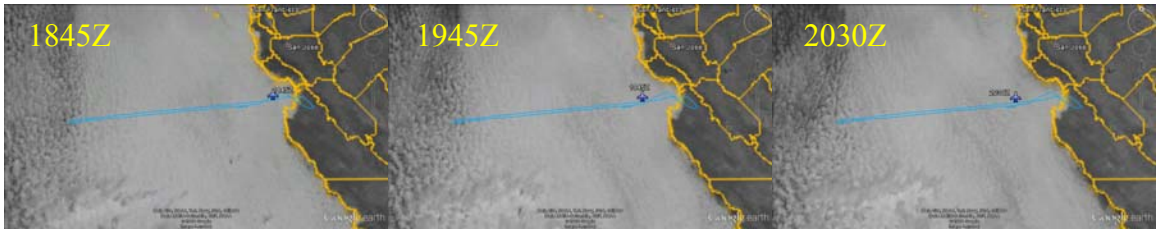

Figure 22. Three sequential GOES-15 visible images on 26 September 2012, at 1845, 1945, and 2030 UTC, respectively, show cloud variability during RF10. White lines are the flight track. Plane icon is the location of TO at time of image.

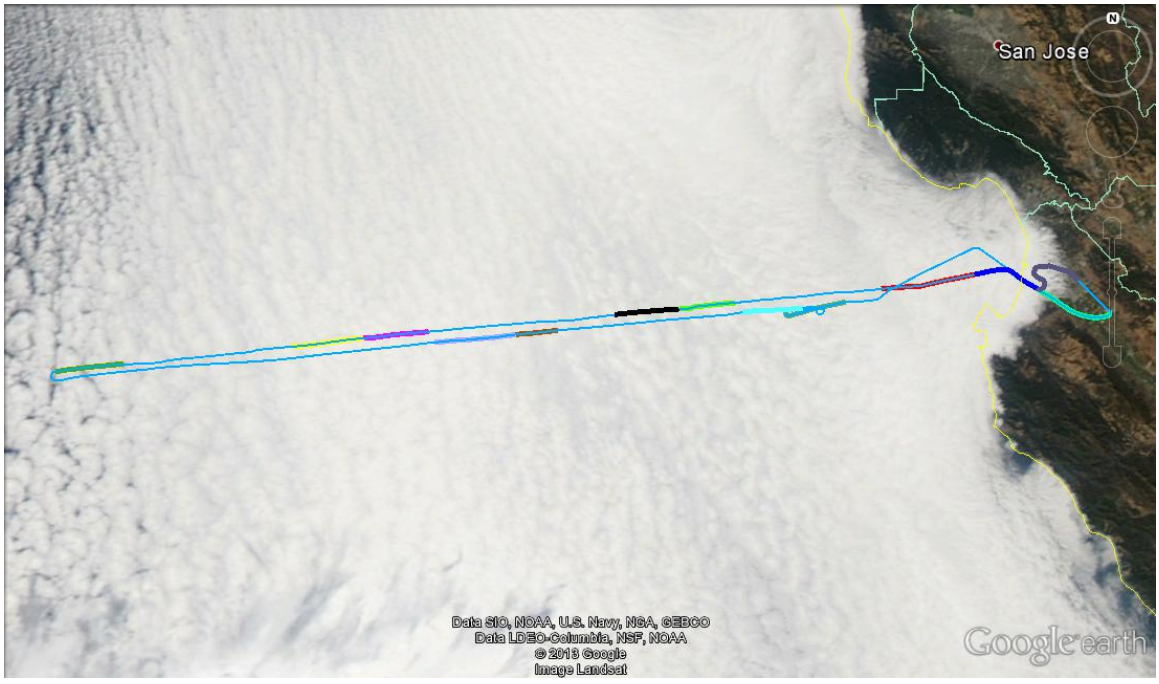

Figure 23. 26 September 2012 MODIS 2145 UTC image overlaid on Google Earth with RF10 flight track (blue solid line) and FS1-FS13. The color here for the flight track of each profile is the same as shown in Figure 24.

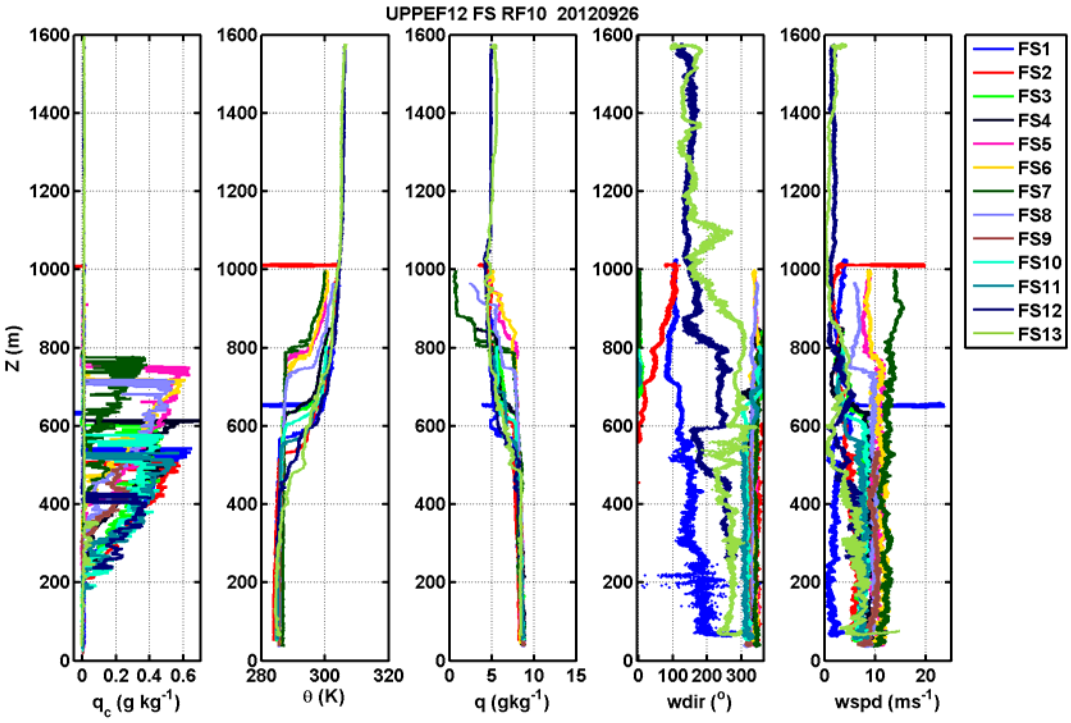

Figure 24. Same as Figure 19, except for soundings of RF10.

The q_c, θ, q, wind speed and direction for each of the 13 full soundings are plotted in Figure 24. The vertical profiles of q_c show the thickest cloud of all UPPEF 2012 cases with maximum cloud thickness approximately 330m. The highest cloud top was at 780m at the western most portion of flight track (leg FS7), and the lowest cloud top was at 420m near the coast (FS12). The difference in cloud top heights is 360m, over a distance of approximately 325km. The boundary layer height plot in Figure 25, though based on inversion height, represents the top of the cloud well, since it was solid cloud throughout the flight track. The descending slope of the boundary layer from west to east is well characterized. This slope is quantified using contour plots discussed below.

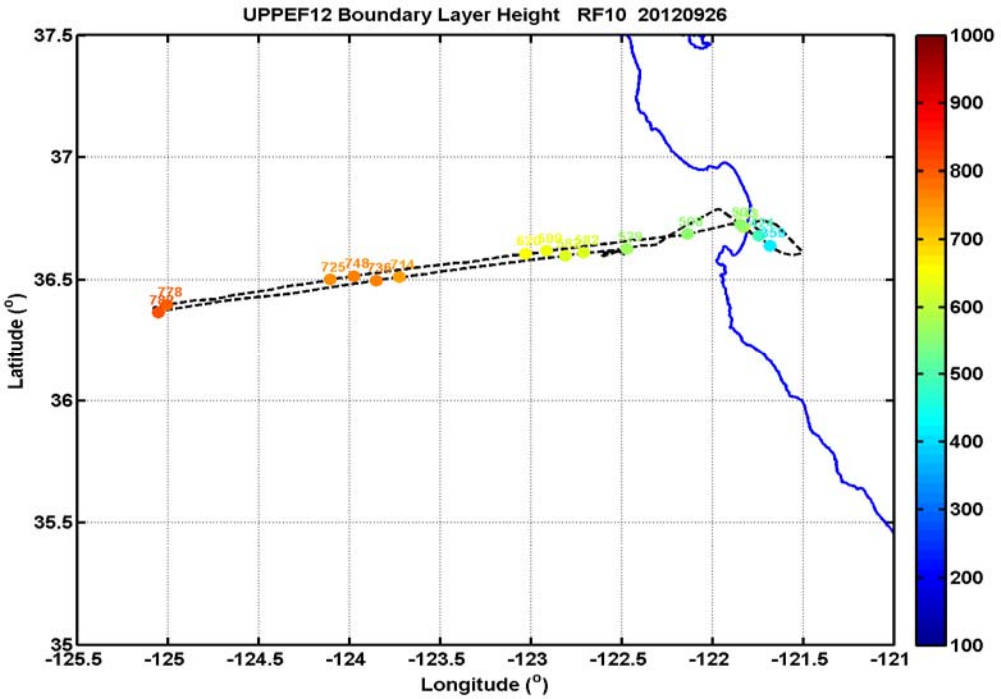

Figure 25. Boundary layer heights for RF10. Dotted line represents flight track. Coloreddots and numbers represent boundary layer height.

All of the full soundings, short soundings, and level legs in RF10 are combined to produce the contour plots in Figure 26. Figure 26a shows solid cloud from all soundings throughout the flight and the solid black line showing the slope of the cloud tops. The same solid black line is also drawn on other subplots to ensure that the boundary layer top seen from all variables are consistent. Figure 26 shows that the slope out to ~123.9W (200 km offshore) is 2 m per kilometer, while it levels off further west at about 0.5 m per kilometer. The cloud thickness is fairly uniform until the westernmost part of the track, beyond which point the cloud becomes broken. The full soundings did not extend as high as in RF02 to allow a detailed representation of the free atmosphere above the BL, but the spatial variability is well shown in the BL. Moisture variability across the boundary layer top varies substantially as seen in Figure 26b. The BL is moist at 9 gkg^{-1}, but the free atmosphere above is not as dry as in RF02, resulting in much smaller moisture jump across the cloud top. At the coast, q decreases more than over the ocean. Moisture is mixed above the BL and for most soundings, q is greater than 5 gkg^{-1}. In comparison, the

q values were all less than 5 gkg^{-1} above the BL during RF02. A vertical profile of θ is shown in Figure 26c. The slope of the potential temperature inversion is consistent with the slope of the cloud top. In the BL, θ is uniform with height, with a strong inversion of about 10K at the BL top. Above the BL, the θ increases to 300-305K. The darker blue is lower values of θ and the red colors are higher values of θ. Finally, Figure 26d is of wind speed. As in RF02, the wind speeds are typically higher in the BL and decreasing above by 2-3 ms^{-1}. The wind is weakest near the coast, at approximately 4-6 ms^{-1}. Offshore, the winds increase to 10-12 ms^{-1}. The slope of wind shear is fairly consistent with the top of the cloud layer, except for at the westernmost portion of the track, where the wind increases slightly above the cloud top.

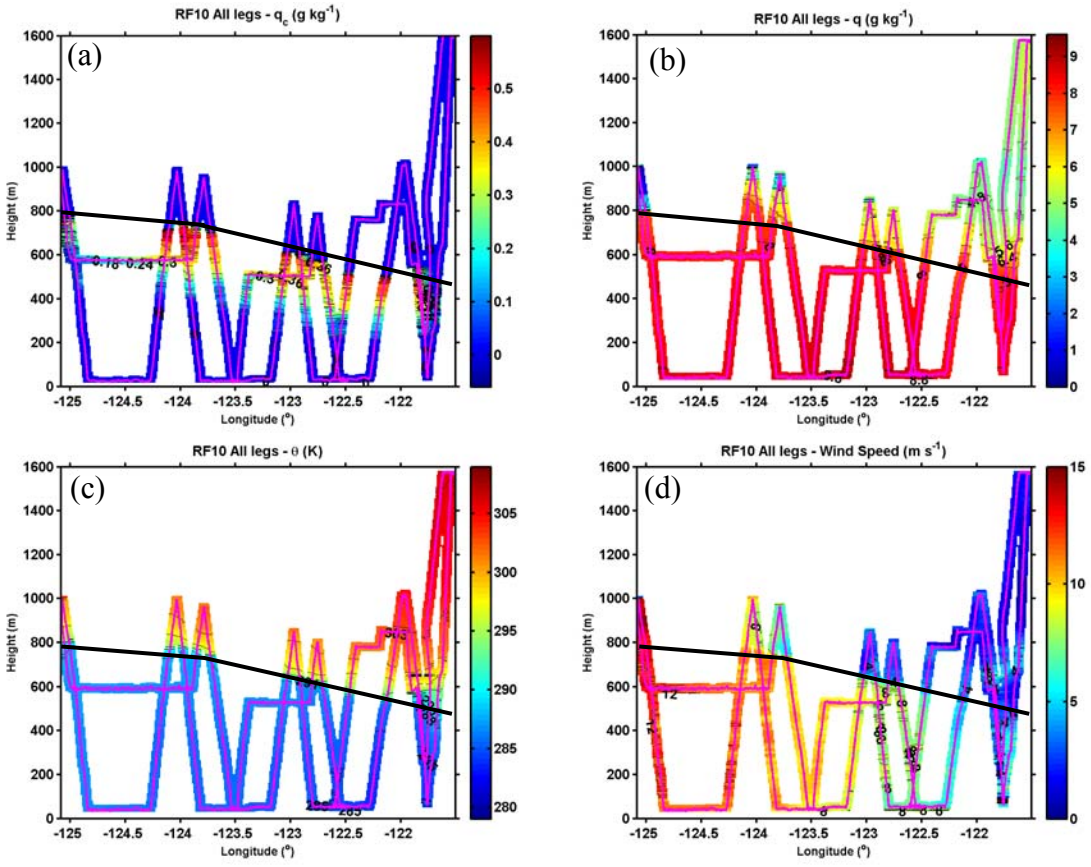

Figure 26. Contour plots for vertical profiles of (a) q_c, (b) q, (c) θ, and (d) wind speed for entire RF10 flight track. Flight track is represented by solid magenta line.

B. SST VARIABILITY AND ITS IMPACT ON LOW LEVEL TURBULENCE

During each of the flights, SST data was collected from the downward looking infrared radiometer. The SST data from the lowest flight levels (below 100m) of the first 10 flights are shown in Figure 27. The range of the SST in all figures is the same as shown in the color bar next to SST from RF10.

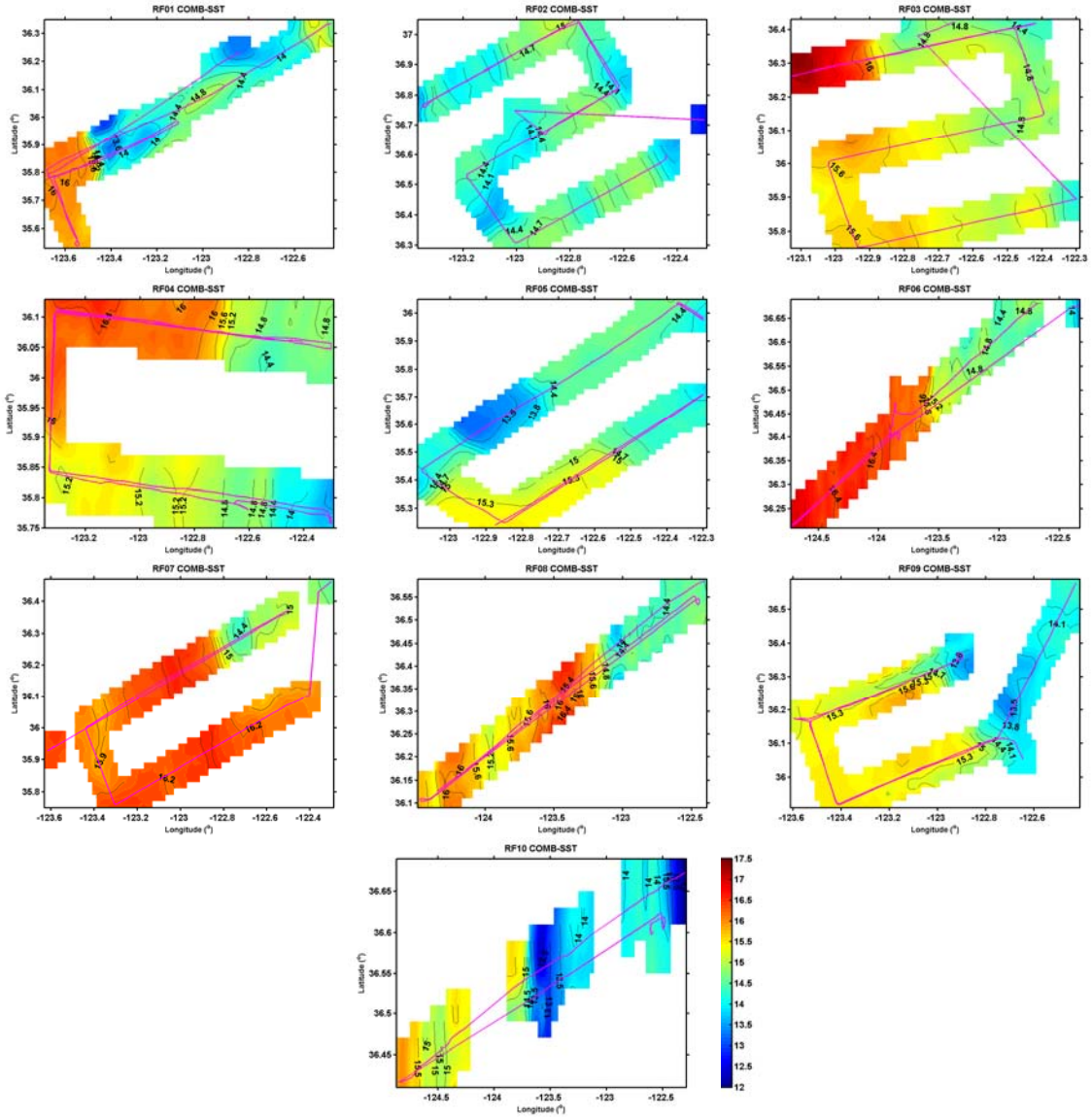

Figure 27. RF01-RF10 contour plot for SST. Solid magenta lines represent level legs at an altitude of 100m or less. SST is in °C.

Figure 27 shows significant spatial and temporal SST variability in the UPPEF 2012 measurement area. The frequent presence of SST front is quite apparent as seen in nearly all flights except for RF02. The magnitude of variability in SST is in general 1–2.5^{o}C. During the first flight, RF01, there was a strong SST front near (35.85N 123.45W). The coldest and rather uniform SST field was observed on RF02 under solid stratocumulus clouds. There was a weak SST front of a 1°C change, near (36.3N 122.9W), during RF03. Another weak front was evident in RF04, near (36.1N 122.7W). During RF05, the northern leg was colder than the southern leg in the U/box-pattern by approximately 2°C. The sixth flight exhibited a 2°C SST change along the surface tracks, but no sharp front was observed. RF07 was primarily in relatively warm SST, near 16°C. The middle of RF08 had SST greater than 16°C, surrounded by 1°C colder SST to the southwest and 2°C colder SST to the northeast. There is a weak SST front with a 1°C change in SST during RF09 along the eastern part of the U-pattern, near 122.9W. During RF10, a strong SST front with a 2.5°C change in SST near (36.55N 123.7W) was observed. The sharp SST front during RF01 and its impact on near-surface mean and turbulence are examined in detail, followed with similar discussions on SST fronts during RF03 and RF05.

1. Strong SST Front in RF01

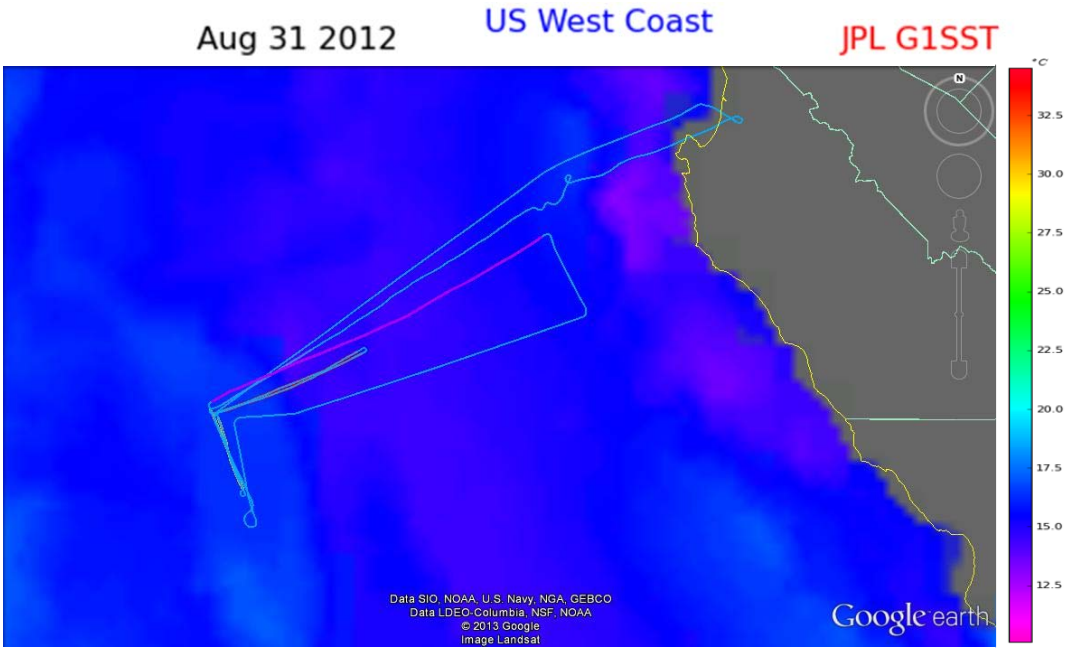

Figure 28. NASA JPL 1km Global SST (G1SST) for 31 August 2012 overlaid on Google earth with RF01 flight track (light blue line), with LL7 and LL12 (purple lines), LL8 and LL9 (orange lines), and LL10 and LL11 (red lines).

A graphical representation of the Global 1 km SST (G1SST) field provided by the National Aeronautics and Space Administration (NASA) Jet Propulsion Laboratory (JPL) at California Institute of Technology's Regional Ocean Modeling System (ROMS) group for the gap-free blended SST along the US West Coast was downloaded for each UPPEF 2012 flight. The image for 31 August 2012 is overlaid in Google Earth with the RF01 flight track and level legs in the cold and warm sectors of the SST front (Figure 28). The sharp SST front is evident in the image along the red and purple legs and corresponds to the SST front revealed by the UPPEF 2012 data (Figure 29). Two levels of legs were flown over the SST front, LL9 and LL10 were flown just under 100m, while LL7, LL8, LL11, and LL12 were flown closest to the surface (~30m). Time series of SST, θ, q, wind speed, wind direction, and pressure comparing the four legs are shown in Figure 30.

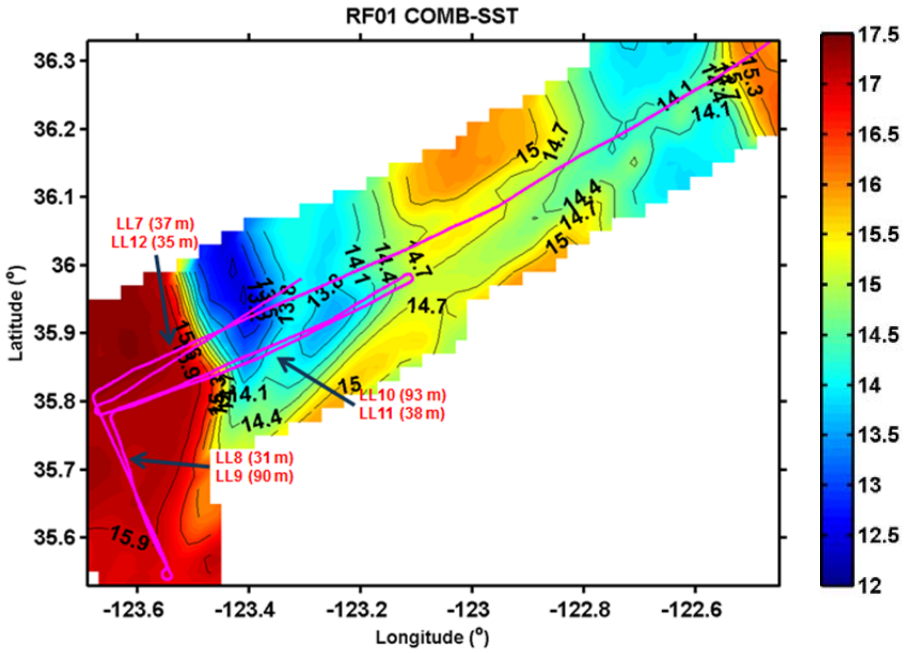

Figure 29. Contour plot for SST during RF01. Flight tracks are represented by magenta solid line. Near surface LL7, LL12, LL10 and LL11 crossed over the strong SST gradient. Near surface LL8 and LL9 are in the warm SST region, as indicated.

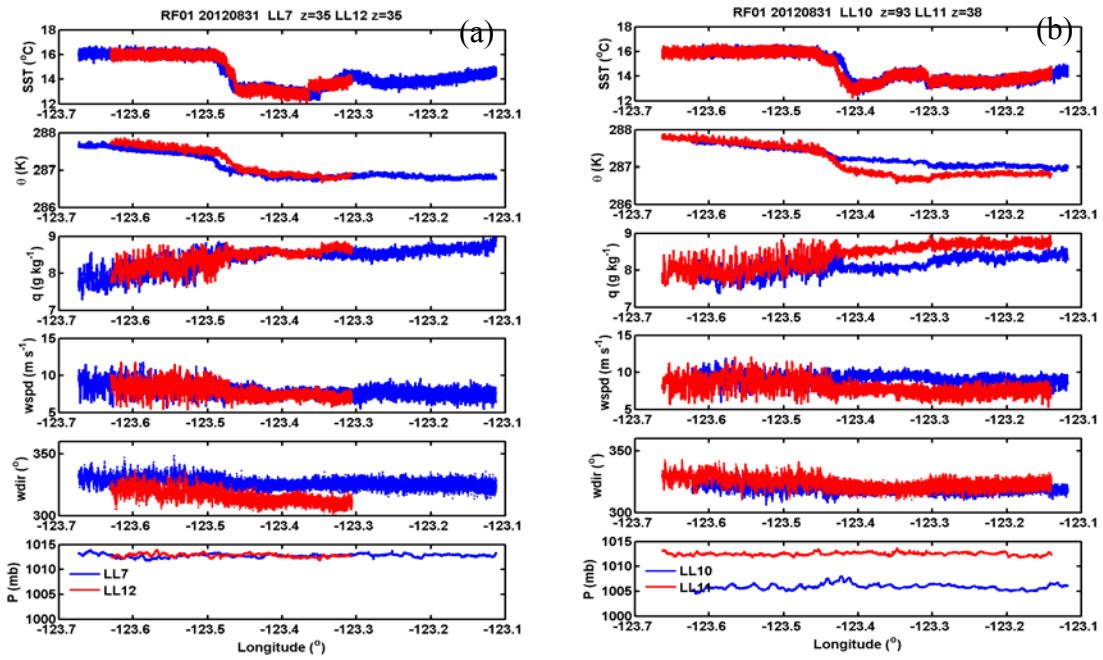

Figure 30. Time series of SST, θ, q, wind speed, wind direction, and pressure plotted against longitude for (a) LL7 and LL12, and (b) LL10 and LL11 crossing the SST front.

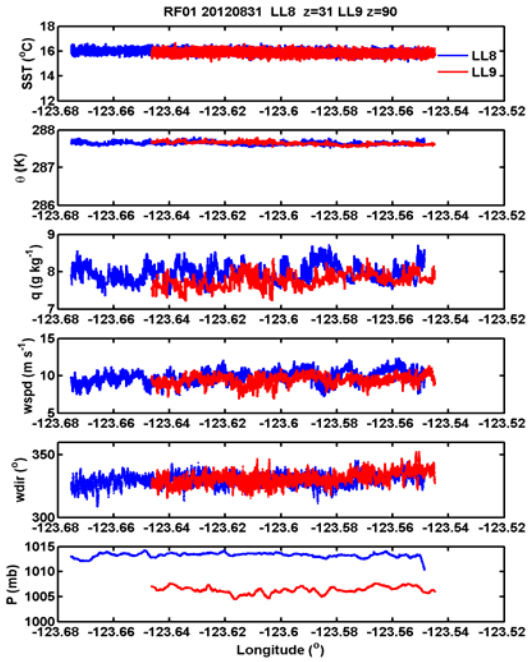

Figure 31. Same as in Figure 30, except for LL8 and LL9 in the warm SST region.

The time series plots are used to compare legs to evaluate temporal and spatial variability of the SST front during RF01 for LL7 and LL12 (Figure 30a), LL10 and LL11 (Figure 30b), and LL8 and LL9 (Figure 31). LL7 and LL12 overlay each other at an altitude of 35m, with LL7 passing the SST front 53 minutes before LL12. LL10 was at 93m and 20 minutes before LL11 at 38m in altitude. Overall, the time series match fairly well for LL7 and LL12, and suggests not much temporal variability for the SST front during the flight, except the wind direction had a more northerly component in LL7. For LL10 and LL11, all variables from the warm sector showed similar magnitude at different height, suggesting that the boundary layer is well mixed to ~100m over the warm water. This is consistent with the results shown in Figure 31, where the entire legs at both levels were from the warm region. Figure 30b indicates apparent stratifications in potential temperature (θ), water vapor (q), and wind speed over the cold water. The section over cold water from the low level (LL11) shows larger specific humidity, colder temperature, weaker winds compared to the respective variables from the layer above, all connected with the cooler surface.

The response of boundary layer turbulence to the significant SST variability is discussed here. In all of the plots, turbulence is greater in the warm SST region (west of front) compared to the cold SST regions (east of front). The sensible heat flux (SHF), latent heat flux (LHF), wind stress, difference of T and SST, and SST for LL7 and LL12 are shown in Figure 32. Similar plots were generated for LL10 and 11 in Figure 33 and for LL8 and 9 in Figure 34. Table 3 provides the calculated mean values of each variable for all relevant legs prepared into warm (top table) and cold (bottom table) regions. A quick glance at Table 3 indicates significant differences in all variables similar to those shown in Figures 30-34. The warm region has near surface (~30 m) SHF in the range of 6-13 Wm^{-2}, LHF of 90-118 Wm^{-2}, and stress between 0.30-0.37 Nm^{-2}, and negative air-SST difference (unstable stratification). In contrast, the cold water region are stably stratified with air-sea temperature difference between 0.6 and 1.8^{o}C, resulting in small but consistently negative SHF at both levels. The wind stress is very weak over the cold water region, too. Latent heat flux are small, too, but consistently positive. Water vapor supply to the boundary layer over the cold region is definitely much weaker compared to the warm region.

Wind speed was observed to be consistently weaker over the cold region compared to its warm neighbor (Table 3). The weaker speed on the cold side of a SST front is primarily due to the stable boundary layer formed over cold SST, which leads to a very shallow BL and thus a strong momentum flux convergence to reduce the wind speed (Skyllingstad et al., 2007). Some flux divergence are seen over the warm water region, the divergence is not apparent over the cold water region, likely imbedded in the sampling error in the fluxes of smaller magnitudes. .

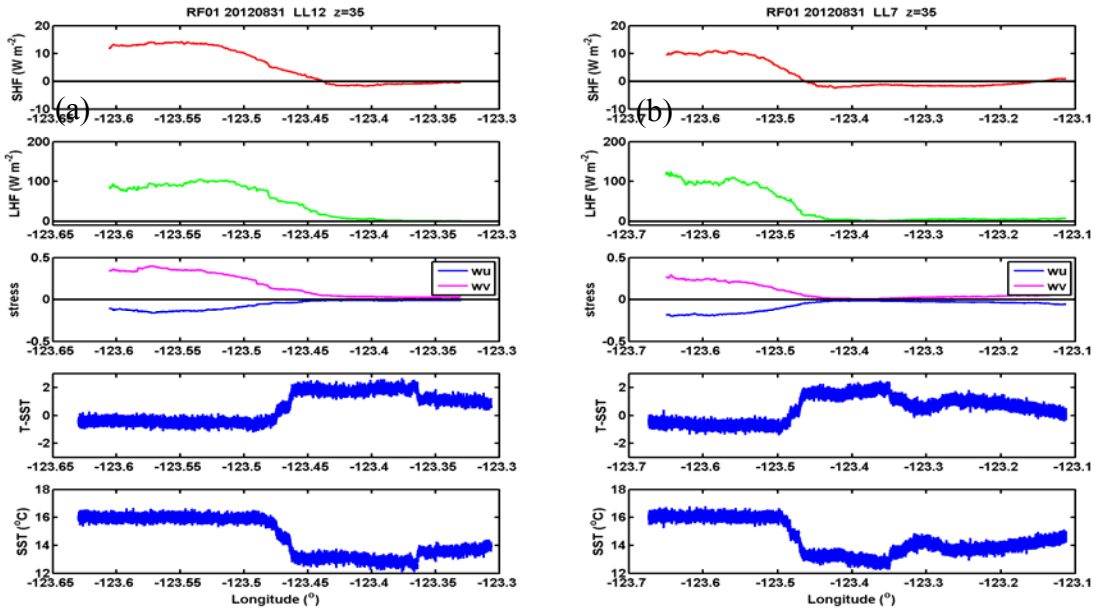

Figure 32. Spatial variability showing SHF, LHF, wind stress, difference of air temperature and SST (T-SST), and SST for (a) LL7 and (b) LL12 crossing the SST front during RF01.

Figure 33 shows the flux variations of air temperature from SST, and SST based on longitude of the overlying LL10 and 11. The main difference between this pair and LL7 and 12 (Figure 32) is the height difference in the level legs. LL7 and 12 were at the same altitude, while LL10 is 55m above LL11. The SST front is located at 123.4W in Figure 33, consistent with Figure 32. The SHF is almost double right before the SST front in the warm sector closer to the surface in LL11, at 123.5W, than at 93m for LL10. The mean values show that the SHF values decrease with altitude, while the LHF remain approximately the same (Table 3). The u-wind stress is also more negative from 123.4–123.5W in LL11, than LL10 as it is approximately zero. The u and v wind stress at the surface nearly reflect each other about the axis for LL11, while the wind stress for LL10 is not symmetric. This wind stress difference is not as evident in the time series plots (Figure 30b) as in the flux plots. The wind backs by 3° as both legs pass the SST front form warm to cold, and decreases in speed by 1.3°C in LL9 and only 0.3°C in LL11 (Table 3).

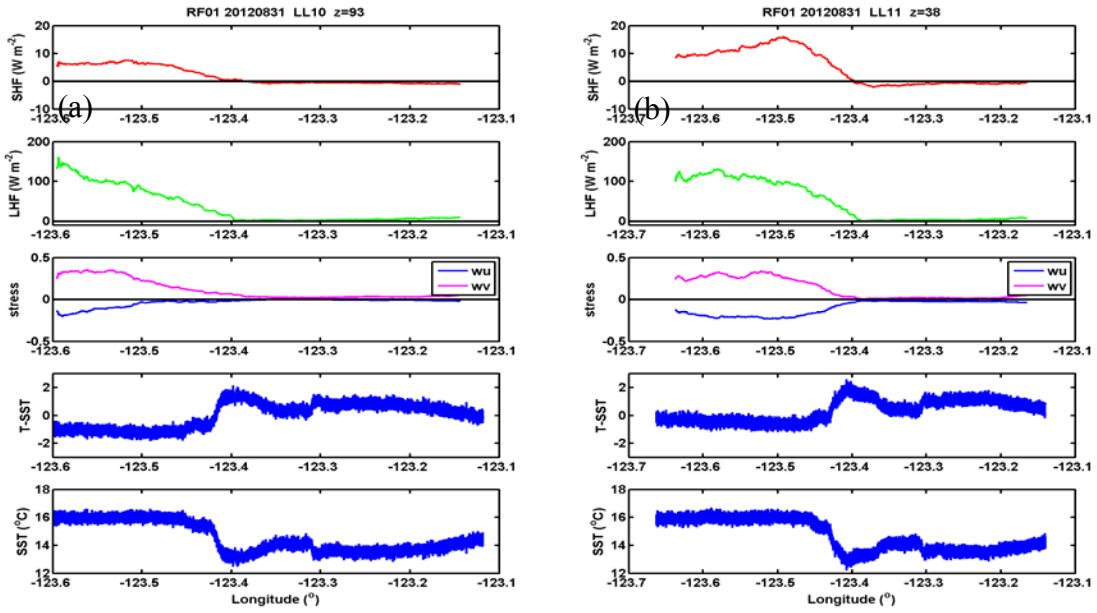

Figure 33. Same as in Figure 32, except for (a) LL10 and (b) LL11 crossing the SST front during RF01.

Figure 34 displays the same plots as Figures 32 and 33, but for LL8 and 9. LL8 and 9 were entirely located in the warm SST region. LL9 was at 90m in altitude, which was 59m above LL8, at 31m in altitude. Both show positive SHF and LHF fluxes, but consistent with LL10 and 11, both fluxes decrease with altitude. The LHF for LL9 is about half of that for LL8 and the SHF is about a third less for LL9 than LL8 (for exact values, see Table 3). The wind stress does not change much, as the wind direction and speed are consistent for both legs. The temperature difference is almost 0.5°C and 0.5K more at 90m than 31m, consistent with LL10 and LL11. The wind speed was stronger for LL8 by at least 0.5 ms^{-1} than all other legs (Table 3). The wind direction is consistent in the warm SST for LL8, LL9, LL7, and LL12.

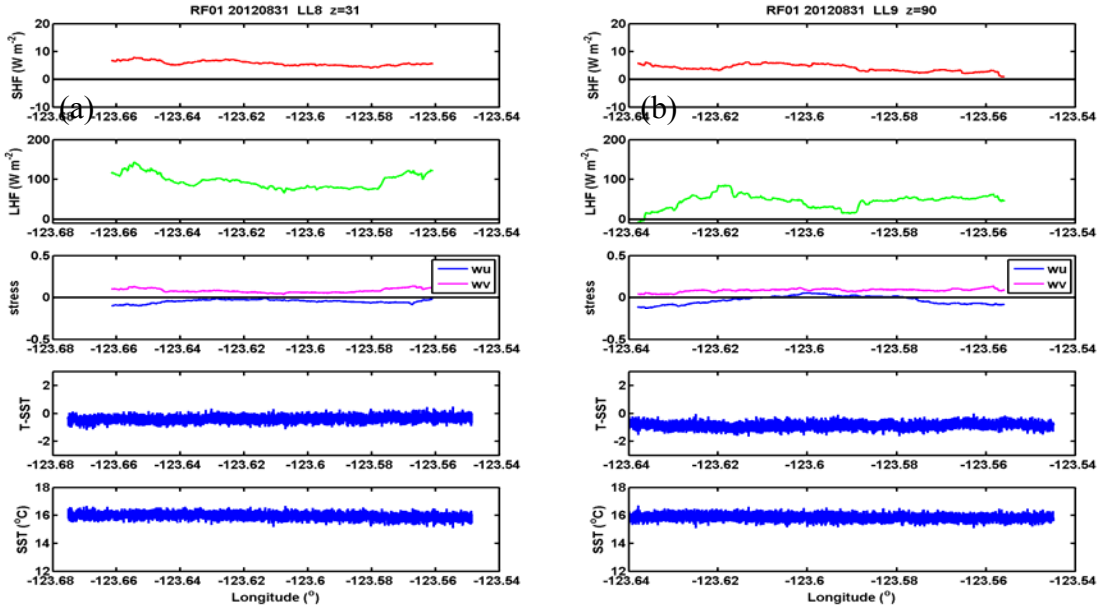

Figure 34. Same as in Figure 32, except for (a) LL8 and (b) LL9 in the warm SST region during RF01.

Table 3. Comparison of mean and turbulent fluxes over warm and cold SST regions.

RF01 Mean variables	LL11 (z=38m) Warm	LL10 (z=93m) Warm	LL7 (z=35m) Warm	LL12 (z=35m) Warm	LL8 (z=31m) Warm	LL9 (z=90m) Warm
SHF (Wm^{-2})	9.0964	6.4384	10.2287	13.2936	5.8609	4.1867
LHF (Wm^{-2})	117.8148	117.1868	104.0729	89.4846	100.1591	43.9612
Stress (Nm^{-2})	0.3621	0.3592	0.2957	0.3741	0.1022	0.1061
Wind Speed (ms^{-1})	8.933	9.3587	8.9654	8.5702	9.9017	9.388
Wind Direction (°)	327.4332	320.9001	329.9618	320.5	329.6294	330.5528
θ -SST (K)	-0.4932	-1.0551	-0.6582	-0.471	-0.3841	-0.8582
SST (°C)	15.9801	15.9686	16.0799	15.9975	15.9687	15.8803

RF01 Mean variables	LL11 (z=38m) Cold	LL10 (z=93m) Cold	LL7 (z=35m) Cold	LL12 (z=35m) Cold
SHF (Wm^{-2})	-0.9813	-0.6611	-1.5665	-1.3253
LHF (Wm^{-2})	3.263	4.5991	4.7319	5.227
Stress (Nm^{-2})	0.0268	0.0319	0.024	0.0352
Wind Speed (ms^{-1})	7.4146	9.0964	7.6675	7.2658
Wind Direction (°)	320.786	317.434	325.0623	312.0479
θ -SST (K)	0.9381	0.6315	1.6552	1.8199
SST (°C)	13.7164	13.758	13.0769	12.977

2. RF03 – Weaker and Warmer SST Front

The third flight, RF03, is another example of measurements over a weaker SST front. The SST remains above 14°C in the cold region, warmer than that found in RF01. The G1SST image overlaid on Google earth with RF03 flight track and front passing legs (LL16 and LL20) highlighted is in Figure 35. The SST variability shown in the G1SST data does not match well with the data collected by the TO in Figure 36. It appears to be about 1-2°C too low and the warm eddy of SST is too far to the west for the G1SST. This is likely associated with the errors in the satellite data. The cloud cover for the third flight was much more extensive than for RF01, which plays a factor in the accuracy of satellite derived SST. Only two level legs collected data from this SST front, LL16 at 35m and LL20 at 92m (Figure 36). There was a 2°C change at SST front, from 15°C to 17°C (Figure 36). Spatial variations of SST, θ, q, wind speed, and wind direction based on the longitude of LL16 and LL20 are also shown in Figure 37. Corresponding flux and flux-related quantities from LL16 and LL20 are presented in Figure 38.

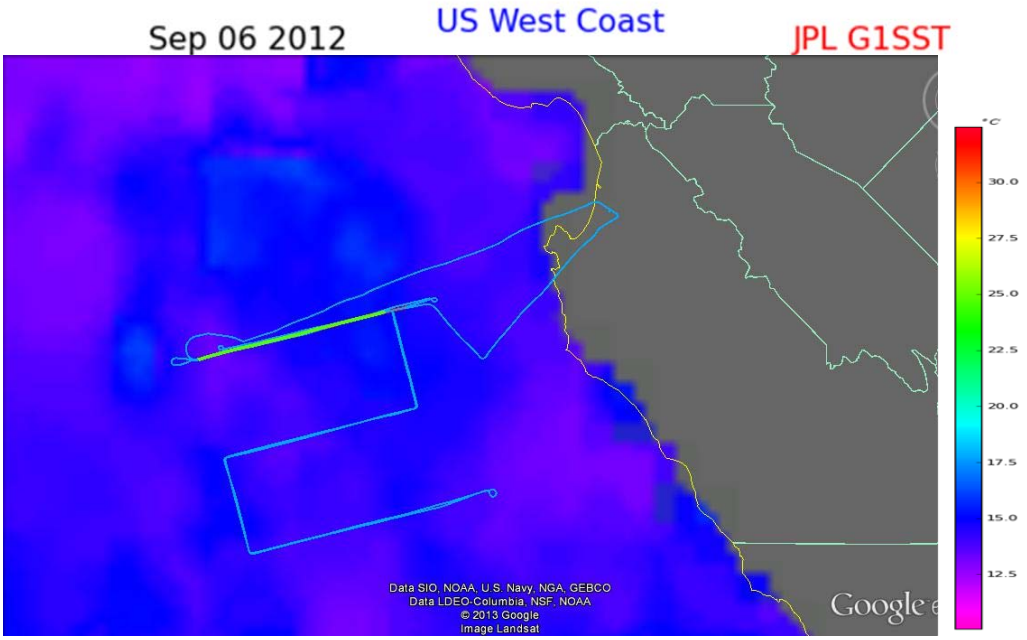

Figure 35. NASA JPL G1SST for 06 September 2012 overlaid on Google earth with RF03 flight track (light blue line), LL16 (green line), and LL20 (red line).

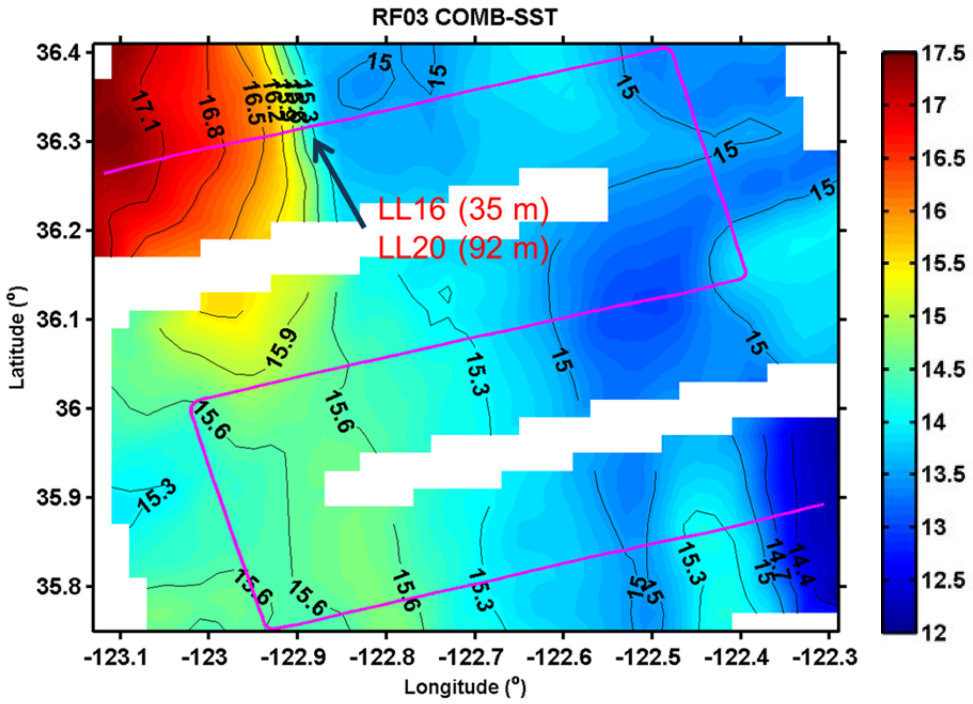

Figure 36. Contour SST plot for RF03. Flight track is the magenta solid line. LL16 and LL20 overlaid each other and crossed over the strongest SST gradient as indicated.

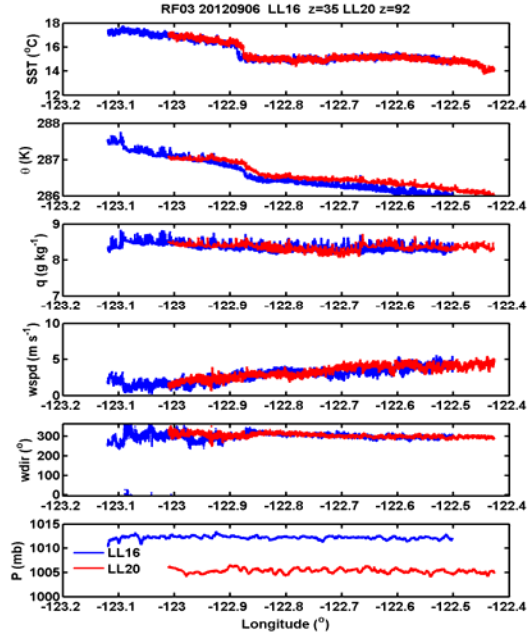

Figure 37. Same as in Figure 30, except for LL16 and LL20 of RF03.

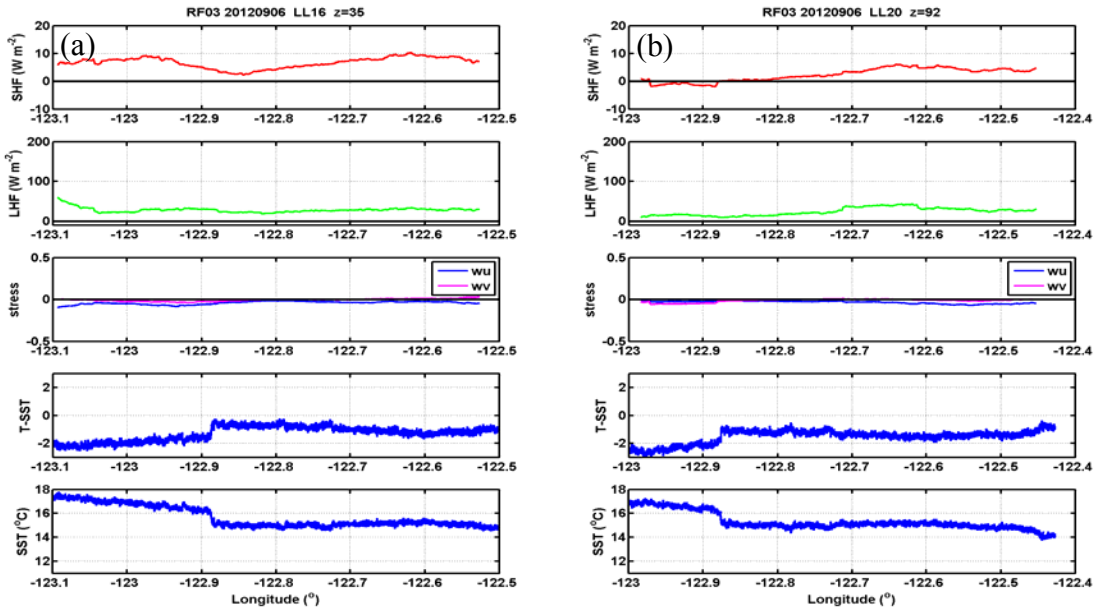

Figure 38. Same as in Figure 30, except for (a) LL16 and (b) LL20 crossing the SST front during RF03.

Figure 36 shows the location of the SST front at (36.3N 122.9W) during RF03. Compared to RF01, the results from RF03 differ significantly. The values for SHF and LHF are positive for the entire leg for LL16 at an altitude of 36m, vice just in the warmer SST region, shown in the results for RF01. The SHF is slightly negative in the warm SST region for LL20 at 92m in height. Once the SST front is passed in the colder SST, the SHF becomes positive—opposite the results of RF01. This is likely due to LL20 being above the surface layer. The surface layer is generally 10% of the BL height. The BL height is approximately 500m over LL20, making the surface layer at 50m in height. The level leg height of 90m is well above the surface layer; other factors than surface forcing is contributing to the negative flux. Also, another difference from RF01 is that the air temperature difference from the SST is negative on both sides of the front. The SST is warmer than the overlying air for both legs, thus should always producing some upward vertical motion and heat fluxes. A third difference from RF01 is that the wind speed is rather light for RF03, less than 5 ms^{-1} during both LL16 and 20, while the wind speed during RF01 was almost double. This light wind speed shows in the nearly zero wind stress, contributing to the low fluxes.

3. RF05 – Gradual SST Change and Cold Eddy

Another interesting flight showing SST variability was RF05. Clouds were primarily solid to broken on 11 September 2012. The SST variability shown in the G1SST image matches fairly well with the TO data (Figures 39 and 40). There was not a single distinct SST front during this flight, but a gradual increase in SST to 15.3°C from the east in the southern legs and the northern legs of the box appear to cross a filament of 13°C (Figure 40). There were four legs that collected data near the surface showing SST variability during RF05. LL9 was at 89m and overtop LL10 at 35m in altitude. LL11 and LL12 were at 33m and 35m, respectively, and were two other surface legs making up the box pattern flown, as shown in Figure 40.

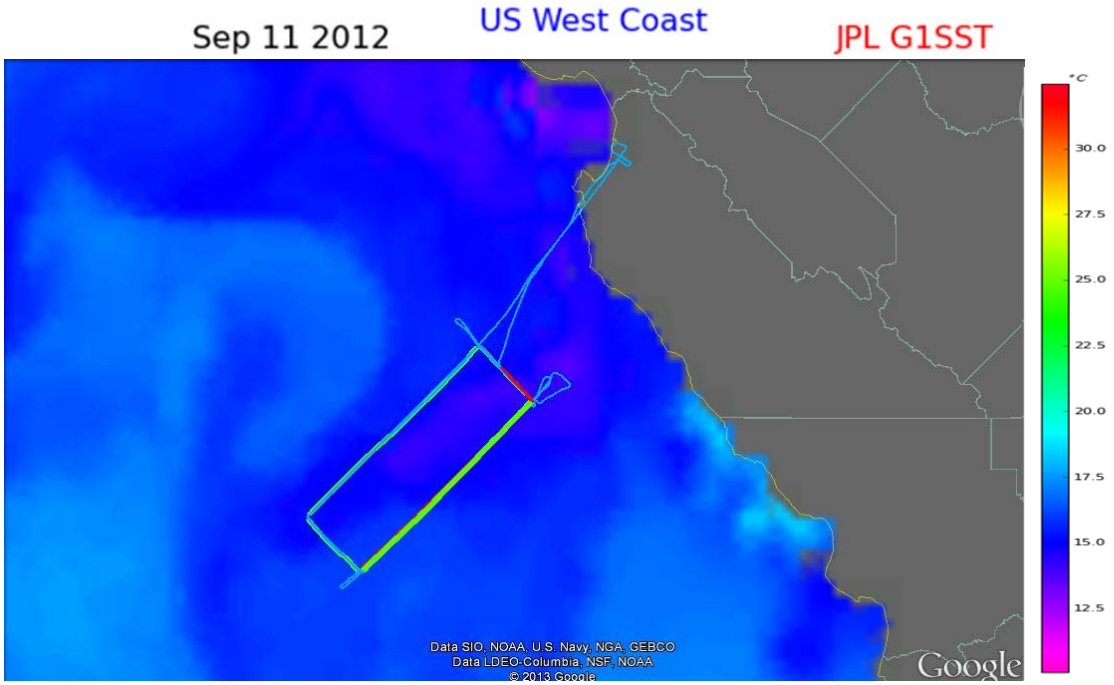

Figure 39. NASA JPL 1km Global SST for 11 September 2012 overlaid on Google earth with RF05 flight track (light blue line), with LL10, LL11 and LL12 (green lines), LL9 and LL13 (red lines).

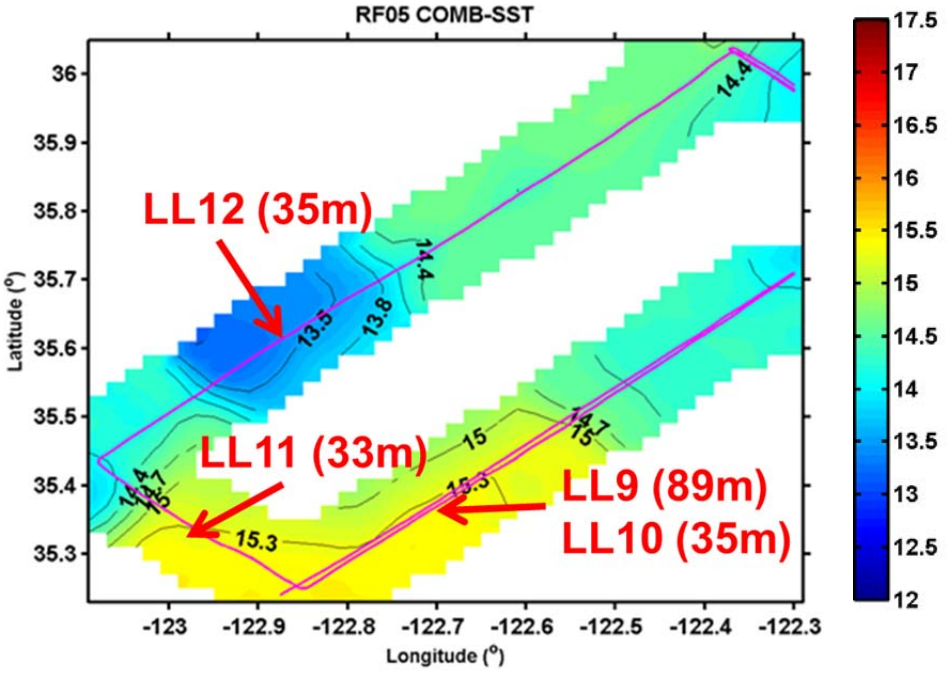

Figure 40. Contour plot of RF05 SST with LL9, LL10, LL11, LL12 and height indicated on the track.

Figure 41 shows the time series of SST, θ, q, wind speed, wind direction, and pressure for the overlying pair (LL9 and LL10), LL11, and LL12. LL9 and LL10 show a gradual decrease in SST to the east towards the coast. LL11 shows a gradual decrease in SST to the northwest, possibly entering a cold filament. Wind is northwesterly between 5-10 ms^{-1} for all four legs, with the wind speed at LL9 slightly higher than the other legs. Wind direction is consistent for all four legs. SST drops by about 1°C in a small portion of LL12 from 122.75W-122.95W from the surrounding SST. Turbulence is evident in SST greater than approximately 15°C. An interesting feature for LL9 and LL10, is that as the SST decreases, θ, q, and wind speed also decrease. These variables contribute to the SHF, LHF, and wind stress profiles for each leg in Figure 42.

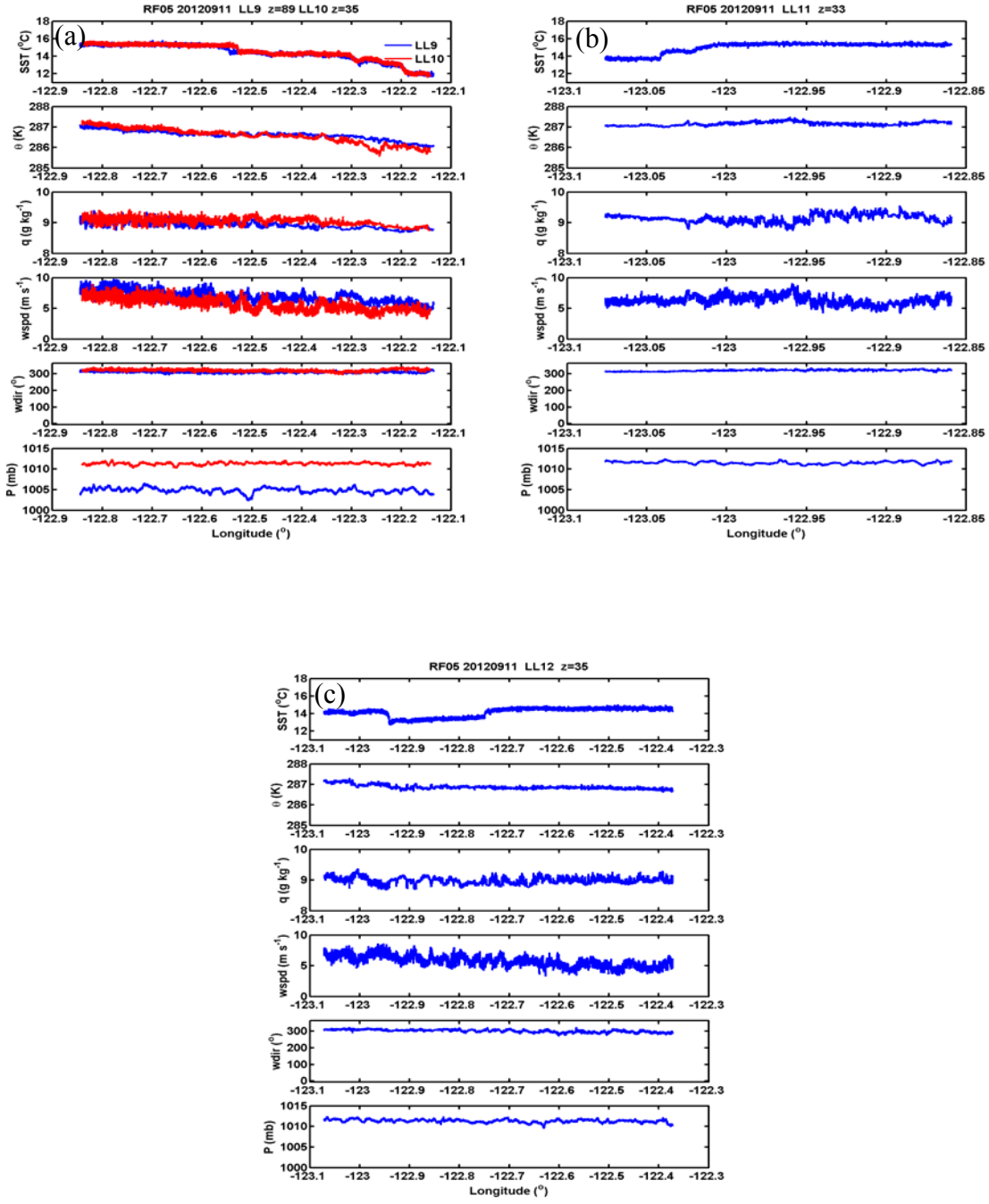

Figure 41. Same as in Figure 30, except for (a) LL9-LL10, (b) LL11, and (c) LL12 of RF05.

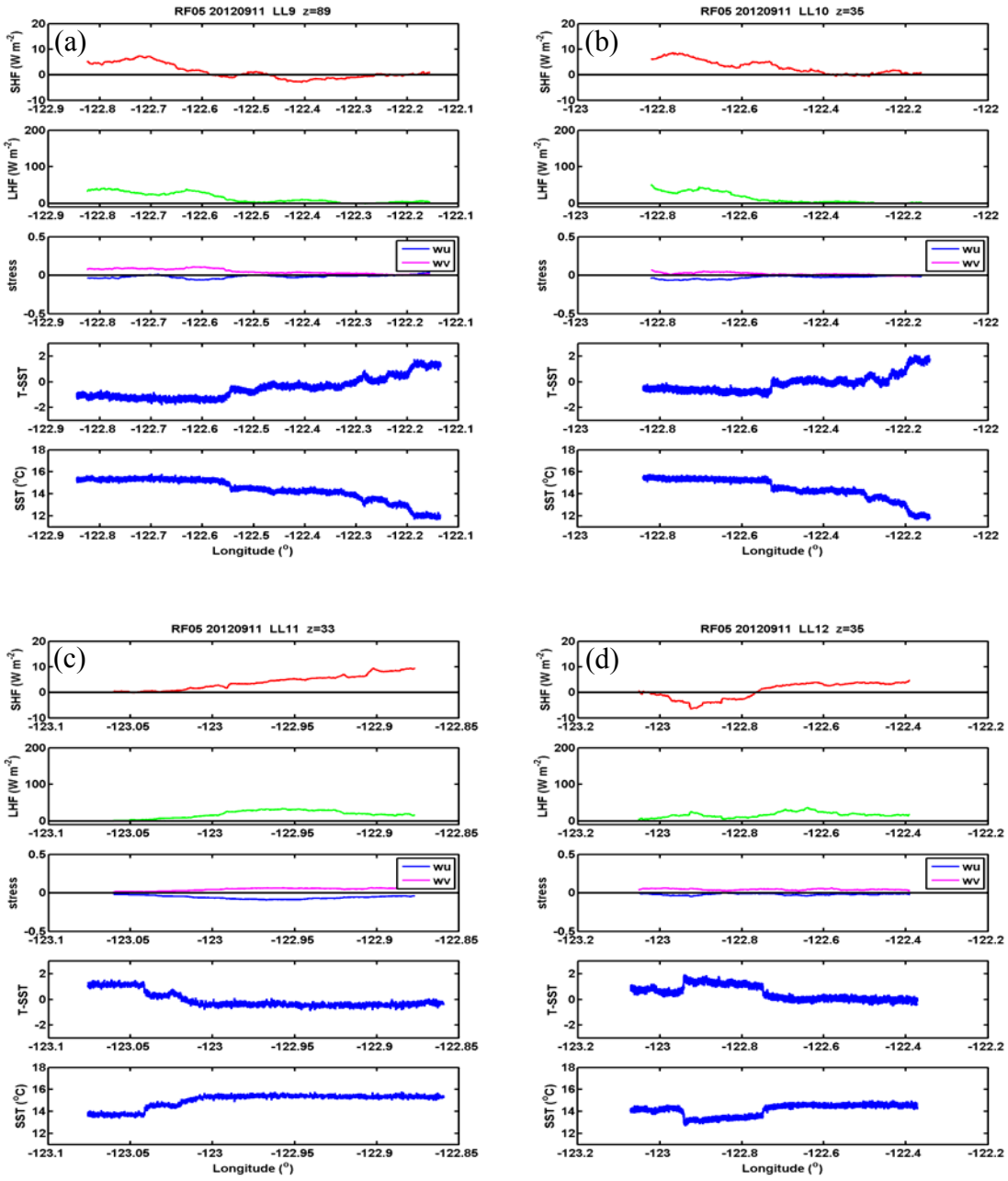

Figure 42. SHF, LHF, wind stress, temperature and SST difference, and SST profiles for (a) LL9, (b) LL10, (c) LL11, and (d) LL12 during RF05.

The SHF variation for all four legs is consistent with the results from RF01. When the temperature difference is negative (unstable stratification), there are positive SHF and LHF. When the difference is positive, then there are no fluxes or they are slightly

negative. The LHF values are very low compared to RF01, along with the wind stress being at a minimum. There are not many differences between LL9 and LL10, except that there is slightly greater wind stress in LL9 than LL10. The results from LL9 at 89m has the same trend as the other legs and RF01, indicating that this leg is possibly in the surface layer. The BL height near LL9 was at 800m. Using the general rule of thumb for the surface layer height at 10% of the BLH, the results suggest that the surface layer may extend up to 90m in height.

C. TURBULENCE CHARACTERISTICS IN CLOUD AND SURFACE

The second flight is a prime example with sufficient level legs to get an accurate depiction of turbulent statistics in solid cloud and its associated boundary layer. The mean data in each level leg is represented by a circle in the flux and variance profiles in Figures 43 and 44. The vertical axes are mean leg height scaled by BLH at the center location of the leg . Figure 43a is the sensible heat flux profile, $\overline{w'\theta'}$, and proportional to the buoyancy flux. Figure 43b is the moisture flux profile, $\overline{w'q'}$, Figure 43a shows that the largest buoyancy flux is in the solid cloud, indicating that radiative cooling in the cloud top is the primary driver of turbulence in the STBL. The surface layer has a small positive buoyancy flux over cold water. Compared to the solid cloud, the surface is not a significant contributor to turbulence in the STBL. However, the surface is the primary source of moisture into the STBL, as represented by the large surface moisture flux in Figure 43b. This figure also shows that there is a significant amount of water vapor flux in solid cloud. The variance profiles for w and θ are shown in Figure 44a and 44b, respectively. Strong turbulent eddies in the cloud layer are shown in Figure 44a. The larger temperature perturbations in Figure 44b, are in the cloud layer. The cold downdrafts originating at the cloud top contribute to large variance. A scatter plot is used to examine how the individual perturbations contribute to the turbulence characteristics. Figure 45 represents the relationship between w' and θ' in solid cloud from an in-cloud leg (LL1) during RF02. The results are oriented in the first and third quadrants, so there are either warm updrafts or cold downdrafts. The scatter plot, along with the individual

probability distribution functions (PDF), however, is strongly negatively skewed and indicates that the cold downdrafts are the primary forcing of turbulence in the cloud.

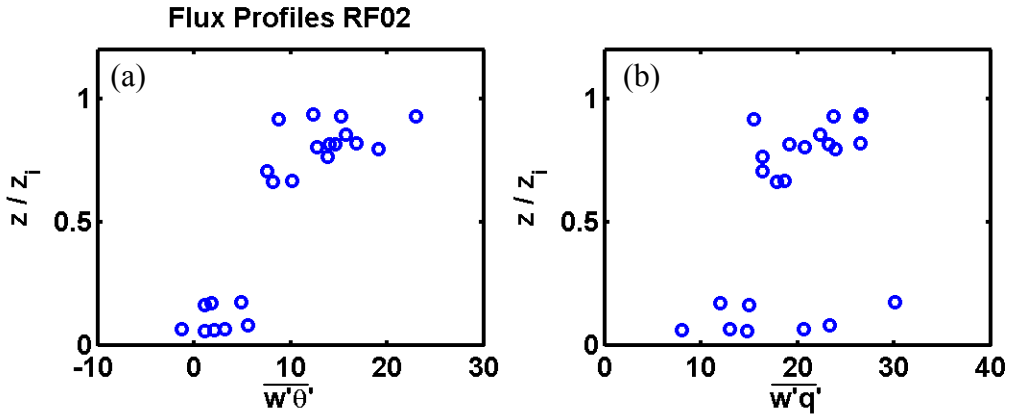

Figure 43. Flux profiles of (a) $\overline{w'\theta'}$ and (b) $\overline{w'q'}$ for RF02. The vertical axis is height scaled by BLH.

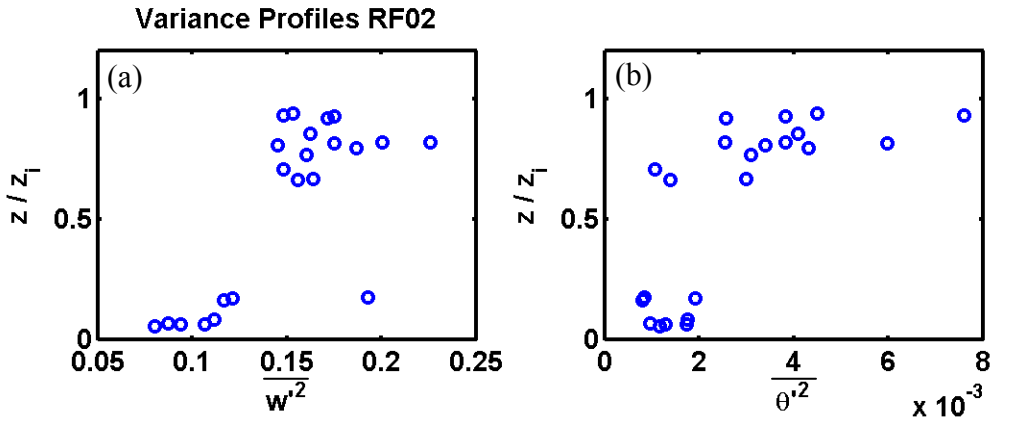

Figure 44. Same as in Figure 43, except for variance profiles of (a) $\overline{w'^2}$ and (b) $\overline{\theta'^2}$ for RF02.

The difference between the contribution from warm SST and solid cloud is significant and is shown in Figure 46. The joint PDF for RF02 in solid cloud is compared to RF01 over the warm SST. Figure 46a shows the PDF for *w'* and θ*'* and Figure 46c is for *w'* and *q'* in the warm SST region of LL11 (LL11W) in RF01. Figure 46b shows the PDF for *w'* and θ*'* and Figure 46d for *w'* and *q'* in the solid stratocumulus cloud during LL1 in RF02. Comparing the PDFs, it can be easily seen that those representing the solid

cloud are negatively skewed (Figure 46b, d) and the PDFs for the legs above the relatively warm SST are positively skewed (Figure 46a, c). The positive skewness indicated warm and moist updrafts from the surface over relatively warm SST. The negative skewness indicated cool and dry downdrafts in the cloud.

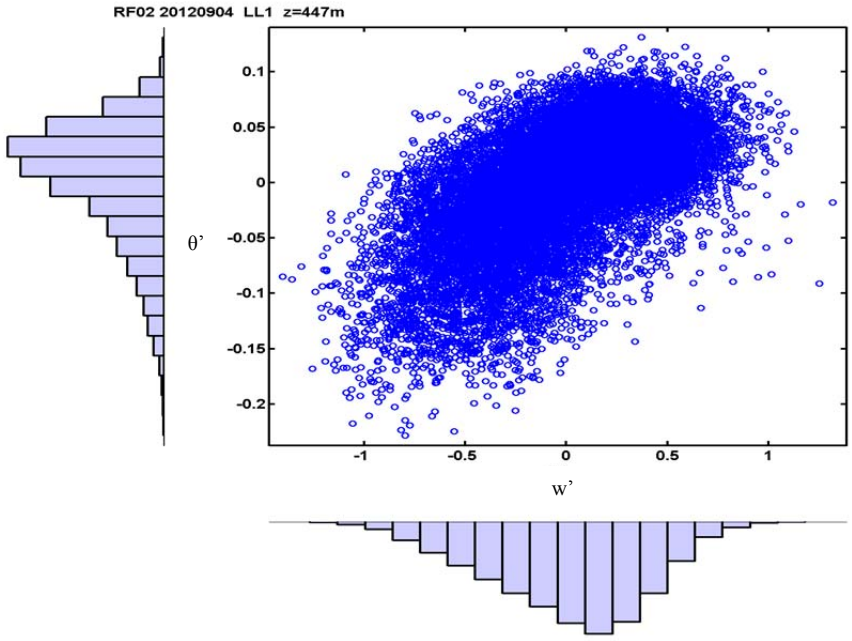

Figure 45. Scatter plot for solid cloud leg (LL1) of *w'* and *θ'* for RF02, showing negative skewness.

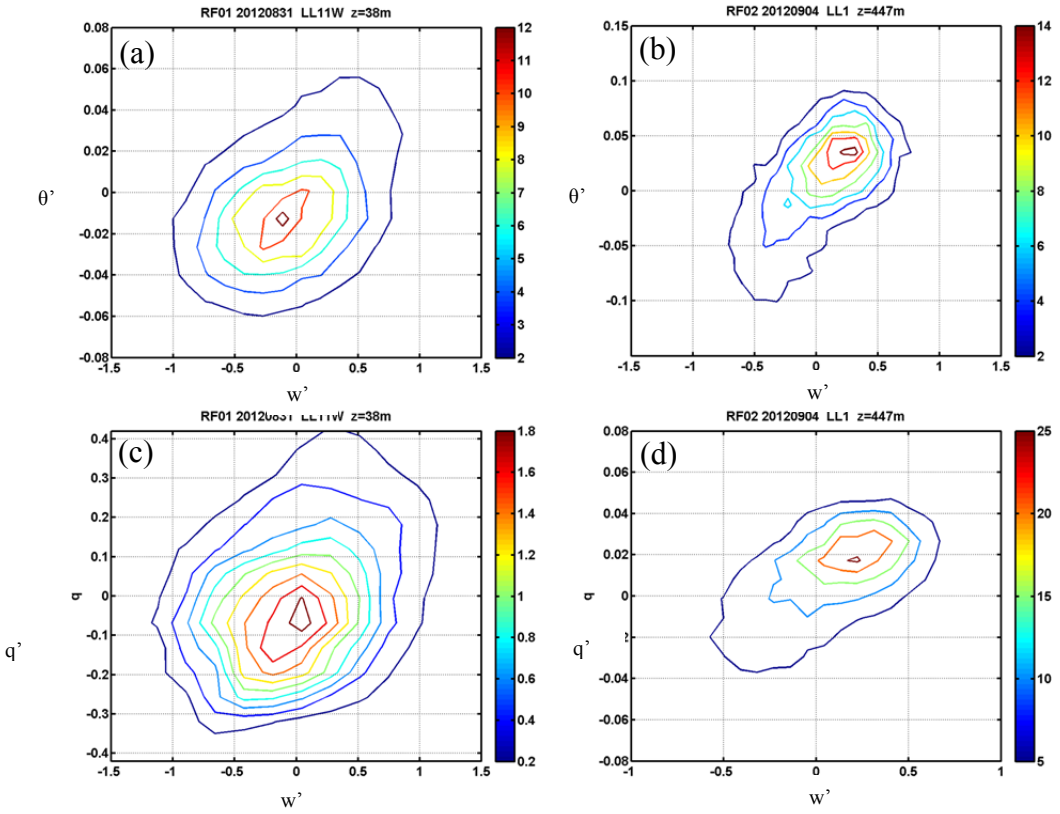

Figure 46. Joint PDF for comparing (a) *w'* and *θ'* for LL11W in RF01, (b) *w'* and *θ'* for LL1 in RF02, (c) *w'* and *q'* for LL11W in RF01, and (d) *w'* and *q'* for LL1 in RF02.

THIS PAGE INTENTIONALLY LEFT BLANK

V. DISCUSSION

A. SUMMARY AND CONCLUSIONS

A major objective of this thesis was to provide the initial analysis of the UPPEF 2012 aircraft measurements by examining all sampled cases and identify specific cases for future in-depth study. In this thesis, the boundary layer heights were estimated for all flights which show a descending slope towards the coast. Two of the flights, RF02 and RF10, were analyzed in depth. Results from these two flights show that the BL decreases at a rate of about 2m km^{-1} to the coast from approximately 200km offshore. Westward of 200km, the slope levels out to a rate of approximately 0.5 m km^{-1}, as seen in the case study of RF10. Conceptually and qualitatively, the boundary layer is easily understood, but accurately quantifying the numerous physical processes that affect the BL is much harder to do. Next, the sea surface temperature variability for each flight was plotted and three flights were chosen to analyze in detail. There was a strong SST front during RF01, a weaker and warmer front during RF03, with a gradual change in SST during RF05. Each of the surface legs covering the changes in SST were evaluated and compared using the spatial variability of relevant variables at different levels. This research found that the small scale variability in the SST resulted in significant variation in the surface exchange of sensible and latent heat fluxes, and wind stress. Such variability makes it difficult to correctly parameterize surface fluxes. The presence of cool downdrafts in the upper cloud layer is evident in the joint probability density distribution and buoyancy flux profiles. The results from this research will guide future cloud parameterization scheme development in forecast models.

B. RECOMMENDATIONS FOR FUTURE RESEARCH

The findings of this initial study yield intriguing results of the boundary layer and its characteristics under solid to broken stratocumulus clouds and in clear conditions. There is a lot of work to be done to further understand the extensive amount of data collected during UPPEF 2012. One such area is in quantifying the entrainment events frequently seen during the initial analyses. There are numerous examples in the data that

show breaks in the LWC, corresponding to breaks in the number of concentration, and decrease in q, amongst others. These breaks are possibly due to the dry downdrafts resulting from entrainment. The EIL in the solid cloud needs to be identified, along with cloud top jumps. Also, there are many interesting features in the cloud from the satellite images. These structures need to be analyzed further to reveal scales of variability in the cloud. Finally, the surface flux parameterization over an inhomogeneous ocean surface needs to be examined in further detail.

LIST OF REFERENCES

Beardsley, R. C., C. E. Dorman, C. A. Friehe, L. K. Rosenfield, and C. D. Winant, 1987: Local atmospheric forcing during the coastal ocean dynamics experiment 1. A description of the marine boundary layer and atmospheric conditions over a northern California upwelling region. *J. Geophys. Res.,* **92**, 1467–1488.

Betts, A. K., 1990: Diurnal variation of California coastal stratocumulus from two days of boundary layer soundings. *Tellus*, **42A**, 302–304.

Bretherton, C. S., B. A. Albrecht, D. Johnson, W. H. Scubert, and A. S. Frisch, 1995: The Atlantic stratocumulus transition experiment – ASTEX. *Bull. Amer. Meteor. Soc.*, **76**, 889–904.

Bretherton, C. S., and R. Pincus, 1995: Cloudiness and marine boundary layer dynamics in the ASTEX Lagrangian experiments. Part I: Synoptic setting and vertical structure. *J. Atmos. Sci.,* **52**, 2707–2724.

Bretherton, C. S., and M. C. Wyant, 1997: Moisture transport, lower tropospheric stability, and decoupling of cloud-topped marine boundary layers. *J. Atmos. Sci.,* **54**, 148–167.

Brost, R. A., D. H. Lenschow, and J. C. Wyngaard, 1982. Marine stratocumulus layers. Part I: Mean conditions. *J. Atmos. Sci.*, **39**, 800–817.

Brost, R. A., D. H. Lenschow, and J. C. Wyngaard, 1982. Marine stratocumulus layers. Part II: Turbulence budgets. *J. Atmos. Sci.*, **39**, 818–836.

de Roode, S. R., and P. G. Duynkerke, 1996: Dynamics of cumulus rising into stratocumulus as observed during the first 'Lagrangian' experiment of ASTEX. *Quart. J. Roy. Meteor. Soc.,* **122**, 1597-1623.

Deardorff, J. W. 1980: Stratocumulus-capped mixed layers derived from a three-dimensional model. *Boundary-Layer Meteor.*, **18**, 495–527.

Flament, P., L. Armi, and L. Washburn, 1985: The evolving structure of an upwelling filament. *J. Geophys. Res.*, **90**, 11765–11778.

Flores, F., R. Rondanelli, M. Diaz, R. Querel, K. Mundnich, L. A. Herrera, D. Pola, and T. Carricajo, 2013: The life cycle of a radionsonde. *Bull. Amer. Meteor. Soc.*, **94**, 187–198.

Hanson, H. P. and P. L. Gruber, 1982: Effect of marine stratocumulus clouds on the ocean-surface heat budget. *J. Atmos. Sci,* **39**, 897–908.

Hegg, D. A., P. A. Durkee, H. H. Jonsson, K. Nielsen, and D. S. Covert, 2004: Effects of aerosol and SST gradients on marine stratocumulus albedo, *Geophys. Res. Lett.,* **31**, L06113, doi:10.1029/2003GL018909.

Hennemuth, B. and A. Lammert, 2006: Determination of the atmospheric boundary layer height from radiosonde and lidar backscatter. *Boundary Layer Meteor,* **120**, 181–200.

Kalnay, E., 2003: *Atmospheric Modeling, Data Assimilation and Predictability.* New York: Cambridge University Press, 341 pp.

Khelif, D., S. P. Burns and C. A. Friehe, 1999: Improved Wind Measurements on Research Aircraft. *J. Atmos. Oceanic Technol.*, **16**, No. 7, 860–875.

Khelif, D., C. A. Friehe, H. Jonsson, Q. Wang, and J. Kalogiros, 2005: Wintertime boundary-layer structure and Air-Sea Interaction over the Japan/East Sea. *Deep Sea Research II*, **52**, 1525–1546.

Klein, S. A., and D. L. Hartmann, 1993: The seasonal cycle of low stratiform clouds. *J. Climate*, **6**, 1587–1606.

Kloesel, K. A., 1992: A 70-year history of marine stratocumulus cloud field experiments off the coast of California. *Bull. Amer. Meteor. Soc.*, **73**, 1581–1585.

Lilly, D. K., 1968: Models of cloud-topped mixed layers under a strong inversion. *Quart. J. Roy. Meteor. Soc.,* **94**, 292–309.

Moeng, C., 2000: Entrainment rate, cloud fraction, and liquid water path of PBL stratocumulus clouds. *J. Atmos. Sci,* **57**, 3627–3643.

Nicholls, S., 1984: The dynamics of stratocumulus: aircraft observations and comparisons with mixed layer model. *Quart. J. R. Met. Soc.*, **110**, 783–820.

Nicholls, S., and J. Leighton, 1986: An observational study of the structure of stratiform cloud sheets: Part I. Structure. *Quart. J. R. Met. Soc.*, **112**, 431–460.

Nicholls, S., and J. D. Turton, 1984: An observational study of the structure of stratiform cloud sheets: Part II. *Quart. J. R. Met. Soc.*, **112**, 461–480.

Nicholls, S., 1989: The structure of radiatively driven convection in stratocumulus. *Quart. J. R. Met. Soc.*, **115**, 487–511.

Pincus, R., M. B. Baker, and C. S. Bretherton, 1997: What controls stratocumulus radiative properties? Lagrangian observations of cloud evolution. *J. Atmos. Sci.*, **54**, 2215–2235.

Seibert, P. F. Beyrich, S. Gryning, S. Joffre, A. Rassmussen, and P. Tercier, 2000: Review and intercomparison of operational methods for the determination of the mixing height. *Atmos. Env.* **34**, 1001–1027.

Seidel, D. J., C. O. Ao, and K. Li, 2010: Estimating climatological planetary boundary layer heights from radiosonde observations: Comparisons of methods and uncertainty analysis. *J. Geophys. Res.,* **115**, D16113.

Sharon, T. M., B. A. Albrecht, H. H. Jonsson, P. Minnis, M. M. Khaiyer, T. M. VanReken, J. Seifeld, and R. Flagan, 2006. Aerosol and cloud microphysical characteristics of rifts and gradients in maritime stratocumulus clouds. *J. Atmos. Sci.*, **63**, 983–997.

Skupniewicz, C. E., J. W. Glendening, and R. F. Kamada, 1991: Boundary-layer transition across a stratocumulus cloud edge in a coastal zone. *Mon. Wea. Rev.*, **119**, 2337–2357.

Skyllingstad, E. D., D. Vickers, L. Mahrt, and R. Samelson, 2007: Effects of mesoscale sea-surface temperature fronts on the marine atmospheric boundary layer. *Bound. Layer Meteor*., **123**, 219–237.

Stevens, B., 2002: Entrainment in stratocumulus topped mixed layers. *Quart. J. Roy. Meteo. Soc.,* **128**, 2663–2690.

Stevens, B., et al., 2003: Dynamics and chemistry of marine stratocumulus – DYCOMS-II. *Bull. Amer. Meteor. Soc.*, **84**, 579–593.

Stull, R. B., 1988: *An Introduction to Boundary Layer Meteorology.* Dordrecht: Kluwer Academic Publishers, 666 pp.

Sun, J., S.P. Burns, D.H. Lenschow, R.M. Banta, R.K. Newsom, R. Coulter, S. Frasier, T. Ince, C.J. Nappo, J. Cuxart, W. Blumen, X. Lee, and X.-Z. Hu, 2002: Intermittent turbulence associated with a density current passage in the stable boundary layer, *Bound. Layer Meteor*., **105**, 199–219.

Sun, J., D. Lenschow, S. Burns, R. Banta, R. Newsom, R. Coulter, S. Frasier, T. Ince, C. Nappo, B. Balsley, M. Jensen, L. Mahrt, D. Miller, and B. Skelly, 2004: Intermittent turbulence in stable boundary layers and the processes that generate it, *Bound. Layer Meteor,*. **110**, 255–279.

Turton, J. D. and S. Nicholls, 1987: A study of the diurnal variation of stratocumulus using a multiple mixed layer model. *Quart. J. Roy. Meteor. Soc.*, **113**, 969–1009.

VanZanten, M. C., B. Stevens, G. Vali, and D. H. Lenschow, 2004: Observations of drizzle in nocturnal marine stratocumulus. *J. Atmos. Sci.*, 62, 88–106.

Wallace, J. M., and P. V. Hobbs, 2006: *Atmospheric Science, An Introductory Survey, Second Edition.* Amsterdam: Elsevier Academic Press, 483 pp.

Wang, Q., and B. A. Albrecht, 1994: Observations of cloud-top entrainment in marine stratocumulus clouds. *J. Atmos. Sci.,* **51**, 1530–1547.

Wang, Q. and D. H. Lenschow, 1995: An observational study of the role of penetrating cumulus in a marine stratocumulus-topped boundary layer. *J. Atmos. Sci.,* **52**, 2778–2787.

Wood, R., 2012: Review: stratocumulus clouds. *Mon. Wea. Rev.,* **140**, 2373–2423.

Xu, K., Cheng, A., and M. Zhang, 2010: Cloud-resolving simulation of low-cloud feedback to an increase in sea surface temperature. *J. Atmos. Sci.,* **67**, 730–748.

INITIAL DISTRIBUTION LIST

1. Defense Technical Information Center
   Ft. Belvoir, Virginia

2. Dudley Knox Library
   Naval Postgraduate School
   Monterey, California